Geophys. J. Int. (2004) **159,** 253–274 doi: 10.1111/j.1365-246X.2004.02379.x

Systematic analysis of crustal anisotropy along the Karadere–Düzce branch of the North Anatolian fault

Zhigang Peng* and Yehuda Ben-Zion

Department of Earth Sciences, University of Southern California, Los Angeles, CA 90089-0740, *USA.*

Accepted 2004 June 8. Received 2004 May 5; in original form 2004 March 14

SUMMARY

We perform a systematic analysis of crustal anisotropy along and around the Karadere–Düzce branch of the North Anatolian fault (NAF), which ruptured during the 1999 Mw 7.4 İzmit and Mw 7.1 Düzce earthquakes. A method consisting of an iterative grid search for the best shear wave splitting parameters in sliding time windows is applied to ∼22 000 measurements recorded in the 6-month period after the İzmit main shock. Based on objective criteria, ∼6600 measurements are assigned high quality and used for further detailed analysis. Most stations near the rupture zone have fast polarization directions that are parallel to, and change with, the nearby fault strike. The average delay times for ray paths that propagate along the rupture zone are larger than for the other paths. These results suggest the existence of an approximately 1-km broad zone around the Karadere–Düzce branch with fault-parallel cracks or shear fabric. However, some fault zone (FZ) stations record bimodal or scattered polarization directions, while stations near large structural complexities (e.g. branching and offsets) show average fast polarization directions that are almost perpendicular to the local fault strike. The average fast polarization directions from ray paths that propagate inside the Almacik block, south of the Karadere–Düzce branch, are neither parallel to the local fault strike nor to the expected regional maximum compressive stress direction. The large overall spatial variations of the results imply that multiple structures and mechanisms contribute to the observed crustal anisotropy in our study area. Most stations do not exhibit a clear dependency of shear wave splitting delay time with increasing depth and hypocentral distance, indicating that the anisotropy is confined primarily to the top 3–4 km of the crust. Using the observed average delay time at FZ stations and assumed propagation distance of 3.5 km, we estimate the apparent crack density in the damaged shallow FZ rock to be approximately 7 per cent.

Key words: fault zone, seismic anisotropy, shear wave splitting, stress, transform fault.

1 INTRODUCTION

Microcracks in a damaged crustal rock are expected to close preferentially in the direction normal to the maximum compressive stress σ_1. In a strike-slip regime, σ_1 is horizontal and is labelled as σ_H, while the minimum compressive stress is labelled as σ_h. Because the effective elastic properties of rocks depend on the distribution of microcracks (e.g. Nur & Simmons 1969; Nur 1971; O'Connell & Budiansky 1974; Hudson 1981; Lyakhovsky *et al.* 1997), seismic shear waves propagating in the direction of σ_H are expected to travel faster than those propagating in the σ_h direction. The difference in speeds will cause shear waves to separate into fast and slow components, a phenomenon that is termed shear wave splitting. Two routinely determined splitting parameters are the polarization direction of the fast wave (ϕ) and the delay time (δt) between the fast and slow waves.

*Now at: Department of Earth & Space Sciences, University of California, Los Angeles, CA 90095-1567, USA. E-mail: zpeng@ess.ucla.edu.

A model consisting of vertically aligned, fluid-filled microcracks parallel to the σ_H direction is commonly assumed in the analysis of crustal anisotropy (e.g. Crampin 1978, 1987; Leary *et al.* 1990). Detailed studies, however, indicate that the observed ϕ directions often vary over short distances, rather than being parallel to the inferred regional σ_H. These observations reflect heterogeneities in the stress field and/or the rock properties. Plausible sources for such heterogeneities include alignment of cracks in the vicinity of active faults (e.g. Zhang & Schwartz 1994; Tadokoro *et al.* 1999; Zinke & Zoback 2000), intrinsic anisotropy resulting from rock fabric (Kern & Wenk 1990) and preferential mineral alignment (Brocher & Christensen 1990), and remnant features of palaeostress (e.g. Blenkinsop 1990; Aster & Shearer 1992).

Studies on the depth extent of crustal anisotropy based on measured splitting parameters often reach very different conclusions. Peacock *et al.* (1988) and Savage *et al.* (1989, 1990) argue that crustal anisotropy in their study areas must be confined to the upper few kilometres to explain different polarization directions observed at stations located only a few kilometres apart. Zhang & Schwartz

(1994) suggest that seismic anisotropy in the Loma Prieta segment of the San Andreas fault system is no deeper than 2 km. Similarly, Munson *et al.* (1995) indicate that anisotropy is confined primarily to the top 3 km of the crust in southern Hawaii. Liu *et al.* (2004) show that crustal anisotropy around the rupture zone of the 1999 Chi-Chi earthquake is dominated by the top 2–3 km. In contrast, Shih & Meyer (1990) and Li *et al.* (1994) claim to have found clear increase of delay times with increasing propagation distance in the south moat of the Long Valley caldera and the Northern Los Angeles basin in California, respectively, and favour a more pervasive anisotropy than just within a few kilometres beneath the stations. Zinke & Zoback (2000) argue, based on two different stable fast directions at one station, that the upper crustal layer (top 2–4 km) near the Calaveras fault in central California appears to be isotropic.

An effort to clarify the spatial properties and sources of crustal anisotropy requires a systematic analysis of a large data set in a densely instrumented area. In this work, we perform such a study for the region around the Karadere–Düzce branch of the North Anatolian fault (NAF) that ruptured during the 1999 Mw 7.4 İzmit and Mw 7.1 Düzce earthquakes. In particular, we are interested in the subsurface seismic properties in the immediate vicinity of the Karadere–Düzce fault. Ben-Zion *et al.* (2003) inferred from systematic analysis of seismic fault zone (FZ) trapped waves that the NAF in this area has a shallow (order 3 km) seismic FZ waveguide that is approximately 100 m wide and is characterized by intense damage (i.e. low seismic velocity and high attenuation). The results of the present work point to the existence of an ∼1-km-wide belt of strongly anisotropic rock around the seismic trapping waveguide on the Karadere–Düzce fault. The belt of anisotropic rock is confined primarily to the same depth extent (top 3–4 km) of the narrower trapping structure.

In the following sections, we first describe our data set and analysis methodology. Using objective criteria, a quality of either high or low is assigned automatically to ∼22 000 measurements of shear wave splitting parameters. Additional detailed analysis is performed on ∼6600 measurements with high quality. We divide earthquakes within the shear wave window of at least one station into FZ and non-fault-zone (NFZ) groups, based on their relative locations with respect to the surface ruptures of the İzmit and Düzce main shocks. We then present measured splitting parameters for each group separately. Finally, we combine the results from the different groups and discuss possible causes and the depth extent of the observed anisotropy in our study area.

2 DATA

2.1 The seismic experiment

A temporary 10-station PASSCAL seismic network was deployed along and around the Karadere–Düzce branch of the NAF a week after the 1999 August 17 Mw 7.4 İzmit earthquake for approximately 6 months (Seeber *et al.* 2000; Ben-Zion *et al.* 2003). An additional 7 stations operated in the first 2 weeks of the deployment period and were later removed (Fig. 1). All stations had REFTEK recorders and three-component L22 short-period sensors with a sampling frequency of 100 Hz. Three months later, the 1999 November 12 Mw 7.1 Düzce earthquake re-ruptured part of the Karadere segment that failed during the August Mw 7.4 event and extended further east. Our temporary seismic network straddled the rupture zones of both main shocks and recorded approximately 26 000 earthquakes during its operational period (Fig. 1a). The event locations were obtained in several stages, starting with standard HYPOINVERSE determinations (Klein 1978) and continuing with event-dependent station corrections (Seeber *et al.* 2000; Ben-Zion *et al.* 2003). The horizontal location errors are less than 1 km around the centre of the network and 1–2 km near the margins. The vertical errors are somewhat greater. In this study, we focus on data recorded by the three-component short-period instruments at all 17 stations (Fig. 1b).

The surface rupture of the İzmit earthquake changes its strike at both ends of the Karadere segment. Many hypocentres of the İzmit aftershocks are distributed around these two areas and clearly outside the major rupture zone. These events may be associated with secondary cross faults and other regional structural complexities (Seeber *et al.* 2000). The occurrence of the Düzce earthquake changed considerably the locations and other aspects of the seismicity pattern in the area. The aftershocks of the Düzce earthquake were concentrated on both ends of that main shock rupture. Additional details on the experiment and data set are given by Seeber *et al.* (2000) and Ben-Zion *et al.* (2003).

2.2 Data selection

The shear wave splitting analysis is conducted on waveforms generated by earthquakes that are within the shear wave window. To avoid contamination from *S*-to-*P* phase conversions near the surface, the incident angle of a ray path must be less than the critical angle $i_c = \sin^{-1}(V_S/V_P)$ with V_P and V_S being the near-surface velocities of *P* and *S* waves, respectively (Nuttli 1961; Booth & Crampin 1985). For a homogeneous half-space with a Poisson's ratio of 0.25, the critical angle is $i_c \sim 35^\circ$ (Nuttli 1961). Because the low-velocity, near-surface layer significantly bends ray paths toward the vertical, a straight-line incident angle of 45° is adopted as the critical angle in this study (e.g. Shih & Meyer 1990; Cochran *et al.* 2003).

In addition, we check the quality of the recorded three-component waveforms and reject those with bad channels. We do not use ∼1400 waveforms observed by station CH from 1999 September 18 to October 7 because the east component was not recorded properly during this period. Approximately 500 waveforms recorded by station GE are not used because the east component did not function well during 1999 August 27 and October 31.

2.3 Data grouping

Fig. 1(b) gives locations of approximately 9200 earthquakes that are within the shear wave window of at least one station in our study area. Because seismic waves propagating inside or outside the FZ may sample crustal rocks with quite different properties, we further separate these earthquakes into FZ and NFZ groups, based on their relative locations with respect to the surface ruptures of the two main shocks. This is defined in the following way. The FZ group contains earthquakes that are relatively close to or inside the rupture zone. For the region north of station CH, we use a 5-km-wide box that is centred around the rupture zone and is parallel to the E–W direction (Box A in Fig. 1b). For the region around the 30-km-long Karadere segment, where the fault is dipping approximately 80° to the north (Seeber *et al.* 2000; Ben-Zion *et al.* 2003), we use a 5-km-wide box that is parallel to the ENE direction and centred on the belt of earthquakes in that area (Box B in Fig. 1b). Because the FZ of the Düzce earthquake is dipping ∼65° to the north (Utkucu *et al.* 2003), we increase the width of the selection box to 12 km for earthquakes around station BV (Fig. 1b, Box C). The NFZ group contains earthquakes that are located south of the surface rupture of the two main shocks in the Almacik block and north of Box B. In the following sections, we present splitting measurements for each group separately and discuss the results.

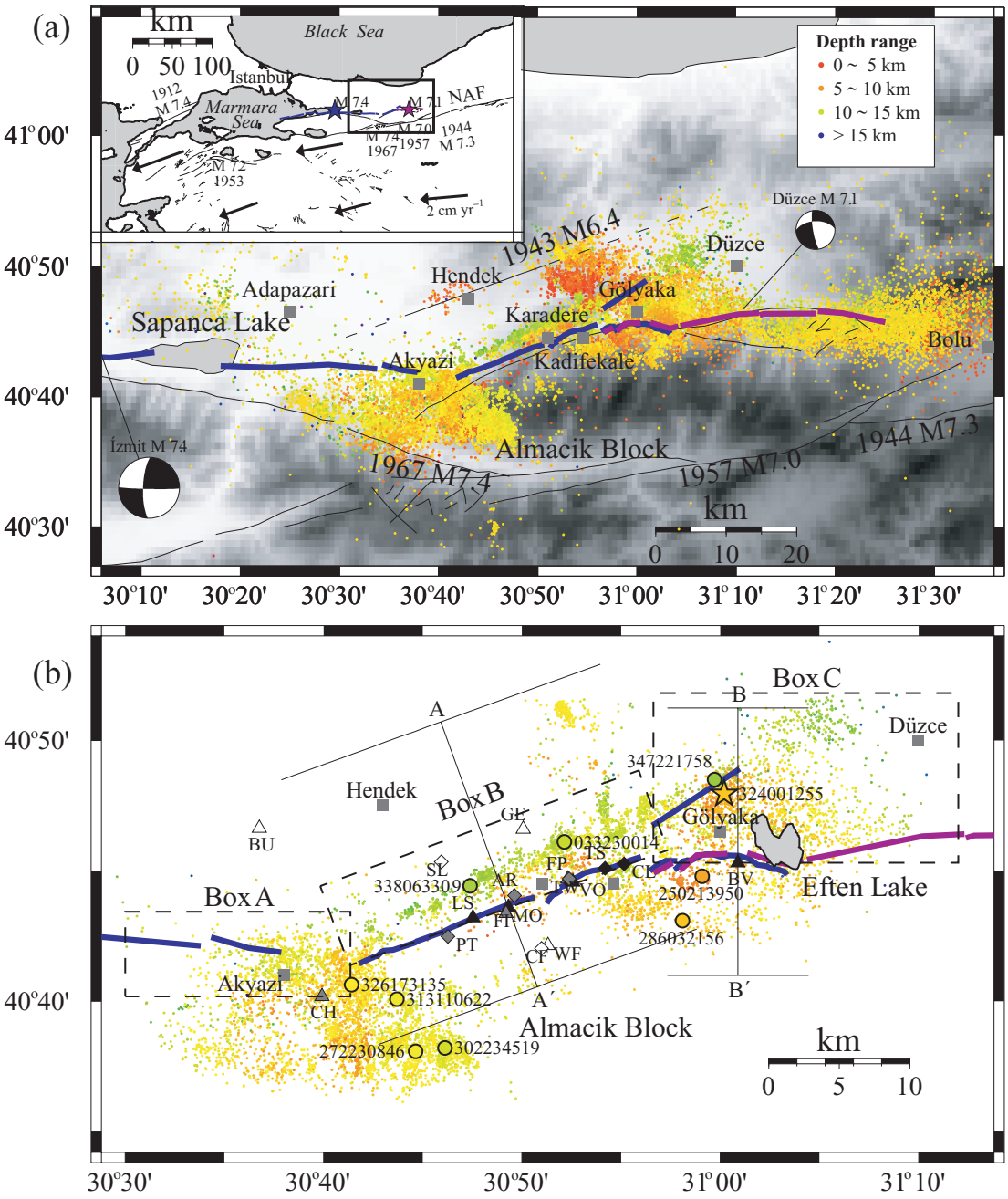

Figure 1. (a) Hypocentral distribution of ∼26 000 earthquakes recorded by the PASSCAL seismic experiment along the Karadere–Düzce branch of the NAF. Aftershock locations are marked with colours denoting different depth ranges. Shaded background indicates topography with white being low and dark being high. The surface ruptures of the İzmit and Düzce earthquakes are indicated with thick blue and purple lines, respectively. Dark thin lines associated with earthquake information denote faults that were active during recent ruptures. Other dark thin lines are geologically inferred fault traces. Grey squares denote locations of nearby cities. The inset illustrates the tectonic environment in northwestern Turkey with the box corresponding to our study area. Arrow vectors represent plate deformation rate (Reilinger *et al.* 1997) from GPS data. Modified from Ben-Zion *et al.* (2003). (b) Distributions of seismic stations and hypocentral locations of ∼9200 earthquakes used for the shear wave splitting analysis in this study. Triangles and diamonds denote stations deployed for approximately 6 months and 2 weeks, respectively. Stations within, near and outside the FZ are shaded with dark, grey and white colours, respectively. Cross-sections along lines AA′ and BB′ are used in Figs 11 and 17, respectively. Earthquakes located within boxes A, B and C denoted by dashed lines along fault strike belong to the FZ group, while the others belong to the NFZ group. Waveforms of the events marked by the star and small circles are shown in Figs 2 and 6, respectively. The event ID numbers consist of the 3-digit Julian day, 2-digit hour, 2-digit minute and 2-digit second of the earthquake occurrence time. Julian days in the range 237–365 are in the year 1999 and those in the range 001–042 are in 2000.

3 ANALYSIS PROCEDURE

Our shear wave splitting analysis consists of two stages. In the first stage, we apply the method of Silver & Chan (1991) assuming a single layer of anisotropy and a sliding window technique to determine the fast polarization direction ϕ and delay time δt of ∼22 000 sets of splitting parameters. In the second stage, we automatically assign a two-level quality to each set of splitting

parameters based on objective criteria and examine details of the results in the higher quality sets. Because the shallow, low-velocity rocks bend the ray paths to the near-vertical direction, most of the seismic energy from earthquakes that are within the shear wave window is in the horizontal-component seismograms. We thus use in the analysis only the horizontal-component seismograms.

We determine the shear wave splitting parameters with the following procedure. First, we construct a 2×2 covariance matrix from the horizontal-component seismograms. Ideally, the eigenvector associated with the larger eigenvalue λ_1 of the matrix points to the initial polarization direction and the smaller eigenvalue λ_2 is zero. In the presences of noise, the latter is small but always larger than zero. The value of λ_2 can be used as a measure of linearity for the shear waves (e.g. Vidale 1986). A grid search is performed over the $\phi - \delta t$ space to find the best solution that minimizes λ_2 and produces the most singular covariance matrix and linear particle motion. In practice, the search range for ϕ is from -90° to 90° in steps of 1°, where the north is at 0° and the clockwise direction is positive. For δt, we use a range of 0 to 0.5 s with an increment of 0.01 s. Once δt is obtained, we correct for anisotropy by advancing the slow component by δt and rotate the fast and slow components into the initial polarization direction α. Ideally, this shifts all the energy to the α direction. The main analysis steps of the above procedure are illustrated in Fig. 2.

Prior to the analysis, the seismograms are low-pass filtered at 15 Hz using a two-way 4-pole Butterworth filter. Because shear waves generated by local earthquakes have a dominant frequency of approximately 5–10 Hz, the applied filter does not degrade the results while helping to suppress high-frequency noise. Next, the seismograms are windowed around the shear wave arrivals. An ideal time window should begin before the fast shear wave arrival and end after the slow direct shear wave arrives, but before the scattered coda waves appear. Because the delay time δt between the fast and slow direct shear waves is different for each seismogram, a window with a fixed start and end relative to the first shear wave arrival is not the best choice for every measurement. Here we automatically determine the position of an optimal window by sliding a 0.6-s time window around the fast shear wave arrival. The best window is picked when the minimum λ_2 solution or the most linear particle motion is achieved (Fig. 3). The routinely picked *S* arrivals may contain various measurement errors. The sliding time window is more flexible than a fixed window in its ability to adjust for errors of phase picks within a certain time range. Measurements from similar earthquake clusters show that with routinely picked *S* arrivals, the splitting parameters determined for different waveforms with the sliding window technique are more consistent than those from a fixed window (Peng & Ben-Zion 2004). The sliding window strategy not only guarantees a best time window for each seismogram, but also provides an effective way for checking the stability of the results in relation to the cycle skipping problem as discussed below.

It is important to provide quality control of the measured splitting parameters to ensure reliability of results. As a result of the very large amount of data in this study, it is not practical to use human interaction for quality control (e.g. Savage *et al.* 1990; Gerst 2003). In addition, a quality assignment based on visual inspection is subjective and the process typically cannot be reproduced by others (Aster *et al.* 1990). Hence an automatic quality assignment using objective criteria is needed. Based on previous studies (Matcham *et al.* 2000; Cochran *et al.* 2003; Gerst 2003), we design the following 10 objective quality criteria and apply them to our data.

(i) The maximum difference of the fast directions ϕ generated by a 0.05-s shift of the best time window is $\leq 30^\circ$.

(ii) The maximum difference of the delay times δt generated by a 0.05-s shift of the best time window does not exceed 0.02 s.

(iii) The difference between the initial polarization α and ϕ is $20^\circ \leq | \phi - \alpha | \leq 70^\circ$.

(iv) The seismograms have a signal-to-noise ratio (SNR) ≥ 3.

(v) The amplitude of the horizontal components is larger than the corresponding vertical component [horizontal-to-vertical ratio (HVR) ≥ 1.5].

(vi) The energy in the waveform component perpendicular to the initial polarization α is small after the anisotropy correction [radial-to-tangential ratio (RTR) ≥ 2].

(vii) The cross-correlation coefficient (CCC) values between the fast and slow components is larger than 0.7.

(viii) The standard deviation of ϕ is $\leq 20^\circ$.

(ix) The standard deviation of δt is less than 0.1 s.

(x) The smaller eigenvalue λ_2 of the covariance matrix is ≤ 0.3.

Solutions that satisfy the above 10 criteria are assigned high quality, while the other solutions are assigned low quality.

The cut-off value for each criterion is chosen to be compatible with previous studies and simultaneously to result in no more than 10–30 per cent of the solutions failing the criterion. Fig. 4 illustrates the distributions of results in relation to the first nine criteria and their relations to λ_2 for all 2818 measurements at station BV. Solutions with high SNR, HVR, RTR and CCC values generally have small λ_2. This indicates that some criteria are not independent. Such dependency provides an additional quality check of internal consistency. Specifically, criteria (i–ii) check the stability of a solution with respect to changes of the selected window to minimize contamination as a result of cycle skipping (e.g. Cochran *et al.* 2003). Criterion (iii) checks the ability of shear waves with certain initial source polarizations to resolve anisotropy. If the initial polarization α of a shear wave is nearly parallel or perpendicular to ϕ, it will not be split into fast and slow polarizations and retain its linear particle motion, resulting in a null measurement (Leary *et al.* 1990; Savage 1999; Gerst 2003). Under such circumstance, the splitting parameters are very sensitive to noise and should be discarded. Cochran *et al.* (2003) reject solutions with α within $\pm 10^\circ$ of their inferred fast or slow directions. However, in the presence of several sets of cracks, resulting in bimodal or scattered values of ϕ, it is not appropriate to apply a global rejection criterion based on the average fast and slow directions. Here we treat each measurement separately and reject (Fig. 5) a solution not satisfying $20^\circ \leq |\phi - \alpha| \leq 70^\circ$, where α and ϕ are the specific values of the initial polarization and fast direction for that measurement. Criteria (iv–v) inspect the three-component seismograms and guarantee that only high-quality data (high SNR) with small *S*-wave amplitude on the vertical component (high HVR) are used (Bouin *et al.* 1996; Gamar & Bernard 1997; Gerst 2003). Criteria (vi–vii) check the waveforms generated by the splitting program and select those solutions with significant energy reduction on the component perpendicular to α after anisotropy correction (high RTR) and a good waveform match between the fast and slow component (high CCC value) (Matcham *et al.* 2000; Cochran *et al.* 2003; Gerst 2003). Criteria (viii–ix) check the existence of a single small 95 per cent confidence area (Matcham *et al.* 2000; Gerst 2003). Finally, the value of λ_2 provides a quantitative measure of the linearity of the particle motion.

In total, approximately 30 per cent of the calculated 21 774 solutions are assigned high overall quality and used for detailed

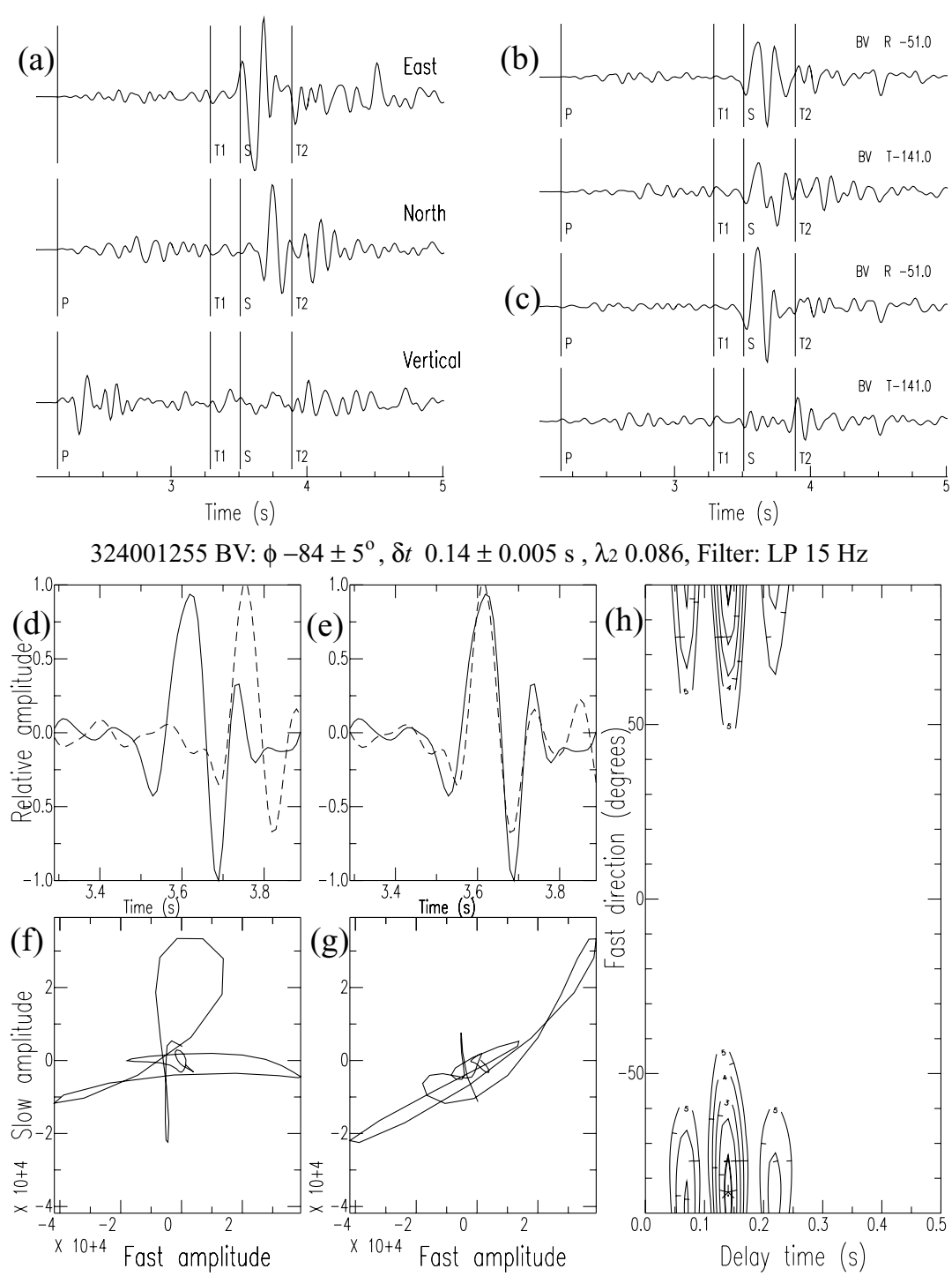

Figure 2. Illustration of steps in the analysis of the shear wave splitting. (a) Three-component seismograms recorded at station BV for event 324001255. The epicentral location is marked as a star in Figs 1(b) and 17. Vertical lines with P, S, T1 and T2 denote the *P*- and *S*-wave arrivals and automatically picked start and end of the time window used in the analysis. (b) Horizontal-component seismograms rotated into the initial polarization and orthogonal directions before correcting for anisotropy. (c) Horizontal-component seismograms shifted in time for anisotropy correction and rotated into the initial polarization and orthogonal directions. The event ID, station name, epicentre distance (Dist), backazimuth (BAZ), focal depth, obtained initial polarization direction α, and start and end of the time window (twin) relative to the *S*-wave arrival are shown at the top of the upper panels. (d) The windowed horizontal components rotated into fast and slow directions. (e) The same waveforms adjusted for the delay time δt. (f) A particle motion plot for the waveforms rotated into the fast and slow directions but before the δt correction. (g) The particle motion plot after the waveforms are rotated and corrected for δt. (h) A contour plot showing the confidence level of the result in the $\phi - \delta t$ space. The best-fit ($\phi = -84^\circ$, $\delta t = 0.14$ s) is marked as an asterisk and the 95 per cent confidence level is shown as a double contour. The event ID, station name, obtained fast direction ϕ, delay time δt, the minimum value of λ_2 and applied filter are shown at the top of the lower panels.

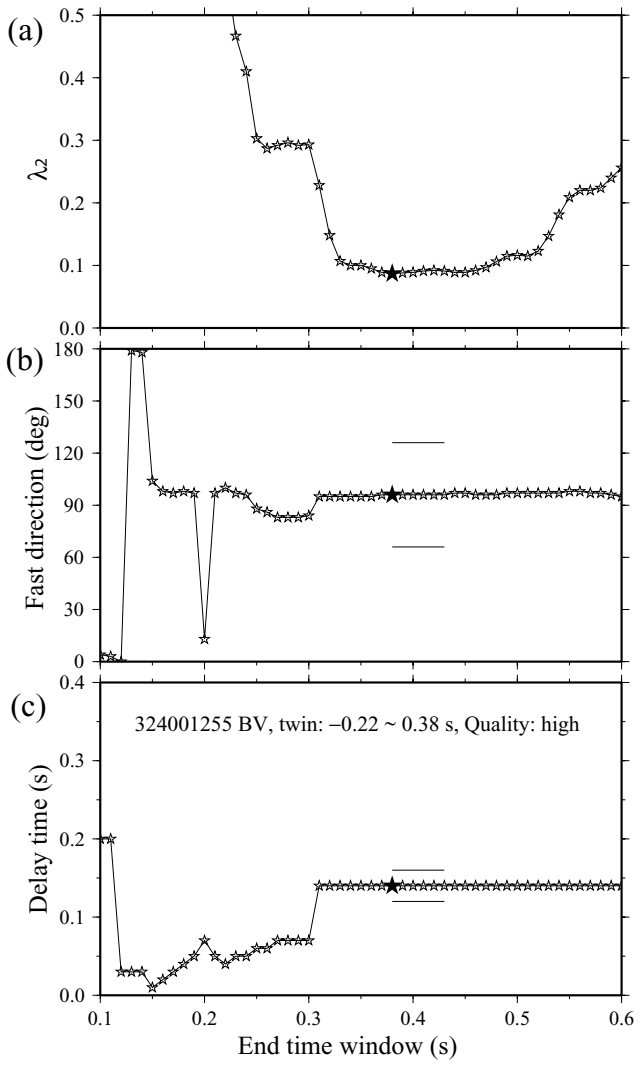

Figure 3. Changes of the (a) smaller eigenvalue λ_2, (b) ϕ and (c) δt with the end of sliding time windows for the shear wave splitting measurement shown in Fig. 2. Stars mark the automatically picked end time associated with the smallest λ_2. Horizontal lines mark $\pm 20^\circ$ of the best ϕ and ± 0.02 s of the best δt that are used to check stability of the solution within a 0.05-s time shift. The word twin stands for the start and end of the determined time window.

examination in the following sections. Slightly different cut-off values may result in different sets of individual measurements being assigned high quality. However, because the results discussed in the following sections are based on statistics of thousands of measurements, the inclusion or removal of a small percentage of measurements in the high-quality set will not change our overall conclusions. As shown in Table 1, the selection reduces the standard deviation of the measured splitting parameters and shifts somewhat the average resolved results (especially for some FZ stations with bimodal distributions of splitting parameters). Fig. 6 shows several sets of original and rotated waveforms used for high-quality determinations of splitting parameters.

4 RESULTS

4.1 Fast polarization direction

The fast directions ϕ of approximately 6600 measurements with high quality at all 17 stations are displayed using rose diagrams in Fig. 7. To provide a statistical analysis of the measured ϕ, we first double each angle and apply the von Mises method to calculate the mean angle θ and a mean resultant length R (Davis 1986; Mardia & Jupp 2000; Cochran *et al.* 2003). The parameter R gives a quantitative estimate of the variance of the directional data, with values near 0 and 1 indicating high scattering and clustering, respectively. As shown in Fig. 7, out of the 17 stations, 9 have R values less than 0.3, indicating that ϕ at these stations are scattered. However, nearby stations have similar rose diagrams, suggesting that the measurements can be used to discern spatial patterns in our area.

4.1.1 Spatial separation

The spatial distribution of the employed earthquakes is complicated, so the observed scattering in Fig. 7 may result in part from ray paths that propagate along regions with different properties. We distinguish between ray paths that propagate inside and outside the FZ by separating both earthquakes and stations into groups based on their relative locations with respect to the active fault. We refer to the 12 stations that are within 1 km of the surface rupture as FZ stations, while the other 5 are named regional stations. We also divide the earthquakes into FZ and NFZ groups according to their hypocentral locations as discussed in Section 2.

4.1.2 FZ group

For earthquakes that are close to or inside the rupture zones of both the İzmit and Düzce earthquakes, 8 out of 12 FZ stations have average fast directions that are parallel or subparallel to the direction of the nearby fault strike (Fig. 8). Station CH is close to the town of Akyazi, where a 5-km-wide surface-rupture gap is observed after the İzmit earthquake. Within this gap, the surface expression of faulting widens into a distributed cracking with nearly zero slip that is hundreds of metres wide (e.g. Hartleb *et al.* 2002). In addition, the rupture trend changes approximately 25° from approximately E–W in the Adapazari basin to ENE along the Karadere segment (Fig. 1). There are 454 individual measurements at station CH for earthquakes around the rupture zone. The mean resultant length R is 0.71, indicating high clustering of the data. The average fast direction θ is approximately 87°, which matches well the average trend of nearby surface rupture expressions. Along the Karadere segment, stations PT, LS and MO have ϕ that are either scattered or bimodal. Their average fast directions are between 100° and 120°. Stations FI and AR have less scattered distributions and their mean fast directions are close to the trending direction of the Karadere segment (∼70° ENE). Stations VO, FP, TW and TS show fairly consistent values of ϕ. The average values are within 20° of the direction of the nearby fault strike. Station CL has a consistent ϕ that is almost perpendicular to the ENE fault orientation. Station BV is near Eften Lake, where the surface rupture of the İzmit earthquake changes its trend from ENE to E–W and terminates. The Düzce earthquake reruptured the easternmost 9 km of the Karadere segment in that area (Hartleb *et al.* 2002). The value of θ is close to 100° for earthquakes that are north of station BV and along the fault dipping direction. This value again matches well the direction of the surface expression of the nearby fault strike.

For stations WF and CF that are located approximately 5 km south of the Karadere segment, we observe bimodal distributions of ϕ. One of the dominant ϕ is approximately N–S. The value of ϕ observed at regional station SL north of the Karadere segment is scattered. Station BU shows fairly consistent splitting results with θ of ∼60°. At station GE, the measured ϕ is slightly bimodal. Approximately

Table 1. Station locations and shear wave splitting results[a].

Station	θ, deg Total	R Total	δt, ms Total	N Total	θ, deg High	R High	δt, ms High	N High	Distance to FZ
CH	79.67	0.45	89 ± 64	3678	82.65	0.62	85 ± 48	1286	<1 km
PT	50.79	0.14	73 ± 55	434	58.92	0.05	72 ± 39	135	<1 km
LS	176.69	0.23	78 ± 57	1966	173.75	0.38	73 ± 38	586	Inside
MO	91.73	0.12	73 ± 55	1778	57.43	0.11	71 ± 45	679	Inside
FI	91.90	0.10	62 ± 46	1895	53.00	0.20	53 ± 35	361	∼400 m
AR	45.48	0.21	84 ± 79	158	43.95	0.29	69 ± 50	60	<1 km
VO	75.04	0.14	71 ± 50	2288	73.81	0.19	73 ± 42	782	Inside
FP	86.50	0.16	71 ± 61	1945	69.20	0.36	79 ± 56	667	∼300 m
TW	110.48	0.10	69 ± 55	398	98.11	0.19	70 ± 50	154	<1 km
TS	126.91	0.15	89 ± 69	134	120.41	0.23	67 ± 37	28	Inside
CL	154.35	0.41	71 ± 41	323	152.68	0.55	82 ± 42	88	Inside
BV	99.80	0.42	89 ± 75	2818	100.44	0.48	84 ± 54	744	Inside
WF	17.36	0.15	65 ± 52	1905	27.28	0.23	68 ± 40	423	∼5 km
CF	125.41	0.07	76 ± 63	335	162.53	0.23	68 ± 40	86	∼5 km
BU	77.09	0.29	91 ± 74	570	61.40	0.35	79 ± 62	172	∼8 km
SL	40.25	0.17	72 ± 69	176	45.37	0.41	43 ± 35	47	∼5 km
GE	110.00	0.36	66 ± 69	973	112.59	0.40	52 ± 53	303	∼5 km

[a] θ is the average fast direction, R is the mean resultant length, δt is the average delay time and N is the number of shear wave splitting measurements. Total and high denote all the measurements and the subset of high-quality measurements at each station, respectively.

40 per cent of the observed ϕ values are between 90° and 120°. Approximately 30 per cent of ϕ are oriented between 125° and 165°. The average fast direction θ is ∼110°.

4.1.3 NFZ Group

Station CH has very consistent ϕ for earthquakes south of it (Fig. 9). The average value θ is approximately 80°, which is within 10° of the value for earthquakes north of CH (Fig. 8). For the FZ stations along the Karadere segment and earthquakes that are outside the FZ, stations PT, AR, VO, FP and TW have either bimodal or scattered ϕ. Stations LS, MO and FI have fairly consistent ϕ with values of θ ranging from approximately 0° to 40°. Stations TS and CL show θ of ∼145°. Station BV has very consistent fast direction with θ of ∼108° (Fig. 9), which again differs by only approximately 10° from the value for earthquakes north of BV (Fig. 8).

For stations outside the FZ, WF shows fairly consistent fast directions with θ of approximately 30°, which is similar to the value of θ observed at stations LS, MO and FI for the same groups of earthquakes. The observed fast directions at station CF are scattered. At stations BU and SL, the average fast directions are approximately NE–SW. Station GE observes a fairly consistent ϕ of ∼NW–SE for earthquakes that are outside the main shock rupture zone.

4.2 Possible causes of anisotropy

A summary plot of shear wave splitting measurements is shown in Fig. 10. For ray paths that propagate inside the rupture zone, the average fast directions ϕ at most FZ stations are in general parallel to and change with the direction of the nearby fault strike. These results suggest the existence of near-vertical, fault-parallel cracks or shear fabric in the vicinity of the rupture zone. However, the results also indicate significant variations of properties along the fault. FZ stations TS and CL have average fast direction of ∼NW–SE, which is almost perpendicular to the trending direction of the Karadere segment. Because these stations are close to a 400-m-wide compressional step-over east of the town of Kadifekale (Hartleb *et al.* 2002), the observed anisotropy at TS and CL may be affected by strong local structural complexities. Some FZ stations (e.g. LS, MO) observe either scattered or bimodal fast directions for earthquakes that are near the FZ. Stations very close to or inside the surface rupture zone typically record after the direct *S* wave large-amplitude, long-period oscillations that are interpreted as FZ trapped waves (Ben-Zion *et al.* 2003). The trapped waves tend to obscure the direct slow *S*-wave arrivals and may reduce the reliability of the derived splitting measurement at these stations.

Fig. 11 shows the splitting parameters and locations of earthquakes that are within the shear wave windows of the FZ station FP and the regional station GE. We note that the same group of earthquakes along the Karadere segment (the dense cluster at the depth range of ∼12–15 km near the heavy dashed line) produce very different anisotropy results at these two stations that are only ∼5 km apart. The FZ station FP has an average fast direction from these FZ earthquakes of $\theta \approx 70°$, which is very close to the direction of fault strike in this area (inset of Fig. 11a). At station GE outside the FZ, θ from the same group of earthquakes is approximately 110°, a direction that is between the ∼NW–SE direction of the regional maximum horizontal compressive stress σ_H (Bellier *et al.* 1997; Tadokoro *et al.* 2002) and the direction of the nearby fault strike (Fig. 11b). For earthquakes outside the FZ (blue dots in Fig. 11), the observed fast directions at the FZ station FP have a bimodal distribution, with two dominant values close to the fault strike and the regional σ_H directions, respectively. At station GE, the average fast direction for earthquakes outside the fault is ∼120°, close to the regional σ_H direction from NFZ earthquakes.

However, the regional stations BU and SL in the Adapazari basin have fast directions that are NE–SW (Fig. 10) and hence almost perpendicular to the regional σ_H. Because most earthquakes within the shear wave window of these two stations have large incident angles, it is possible that such non-vertical ray paths sample different sets of microcracks. Seeber *et al.* (2000) note that the focal mechanisms of aftershocks in this area are highly diverse, pointing to a strongly heterogeneous stress field that may have been partially created

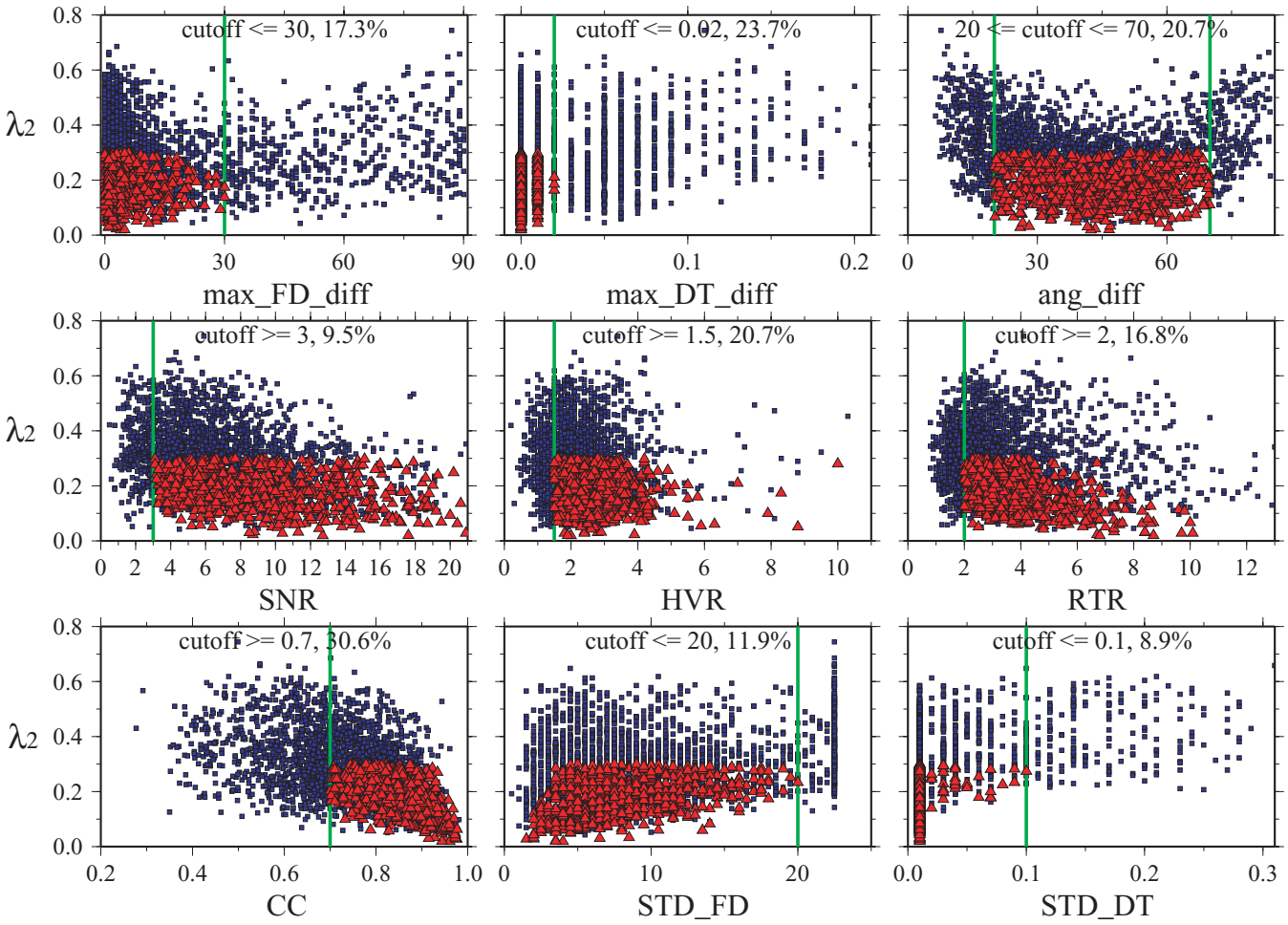

Figure 4. Values associated with the nine criteria against λ_2 for 2818 measurements at station BV. The cut-off values (green vertical lines) and the percentage of rejected solutions for each criterion are given at the top of each panel. Red triangles and blue squares mark measurements that are assigned high and low qualities, respectively. The letter combinations stand for the following: max_FD_diff is maximum difference of fast direction; max_DT_diff is maximum difference of delay time; ang_diff is difference between the initial polarization and fast direction; SNR is signal-to-noise ratio; HVR is horizontal-to-vertical ratio; RTR is radial-to-tangential ratio; CCC is cross-correlation coefficient between fast and slow waves; STD_FD is standard deviation of the fast direction; STD_DT is standard deviation of the delay time.

during the ruptures of the İzmit and Düzce main shocks. Such a heterogeneous stress field may be responsible for generating complex sets of microcracks in the material off the main shock rupture zones.

The average fast directions from ray paths that propagate mostly inside the Almacik block are between 0° and 40°. This range is different from both the inferred σ_H and the direction of the nearby fault segments. The relatively stable Almacik block is assumed to be responsible for the branching of the NAF in this area into two fault strands (e.g. Langridge *et al.* 2002). The southern branch extends along the Mudurnu river valley and broke during the 1944 Bolu-Gerede, 1957 Abant and 1967 Mudurnu Valley earthquake sequences (e.g. Barka 1996; Akyüz *et al.* 2000). The northern one follows the Düzce and Karadere segments and ruptured during the 1999 İzmit and Düzce earthquake sequences. The Almacik block consists primarily of mafic rocks, with some andesitic to basaltic units as well as sedimentary sequences with limestones and shales (Yilmaz *et al.* 1997). Thus, the observed anisotropy within the block is probably caused by lithologic properties such as foliation, bedding, or aligned minerals (e.g. Aster & Shearer 1992) rather than stress-controlled microcracks.

4.3 Delay times and depth extent of anisotropy

As a result of the limited data points and inherent scatter in delay times δt measured using shear wave splitting (Crampin *et al.* 2004), it is very difficult to constrain the depth extent of anisotropy (e.g. Zhang & Schwartz 1994; Cochran *et al.* 2003). Figs 12–15 present for the 17 stations approximately 6600 δt measurements versus depth and hypocentral distance of earthquakes that are either inside or outside the FZ. We also calculate the correlation coefficients (CC) of δt with depth and distance. As shown, most stations have CC less than 0.3, indicating a lack of clear dependency of δt on increasing depth and/or distance. The results suggest that the observed shear wave splitting in this area is primarily caused by shallow structures rather than pervasive anisotropy throughout the entire crust. Because the depth of most earthquakes is larger than 5 km (Seeber *et al.* 2000; Ben-Zion *et al.* 2003), we cannot provide a detailed picture of anisotropy variation with depth in the upper few kilometres. However, δt on the order of 0.1 s is observed for the shallowest earthquakes with hypocentral depth of 3–4 km, suggesting that the anisotropy is confined primarily to the top 3–4 km of the crust. This result is compatible with those found in the Loma

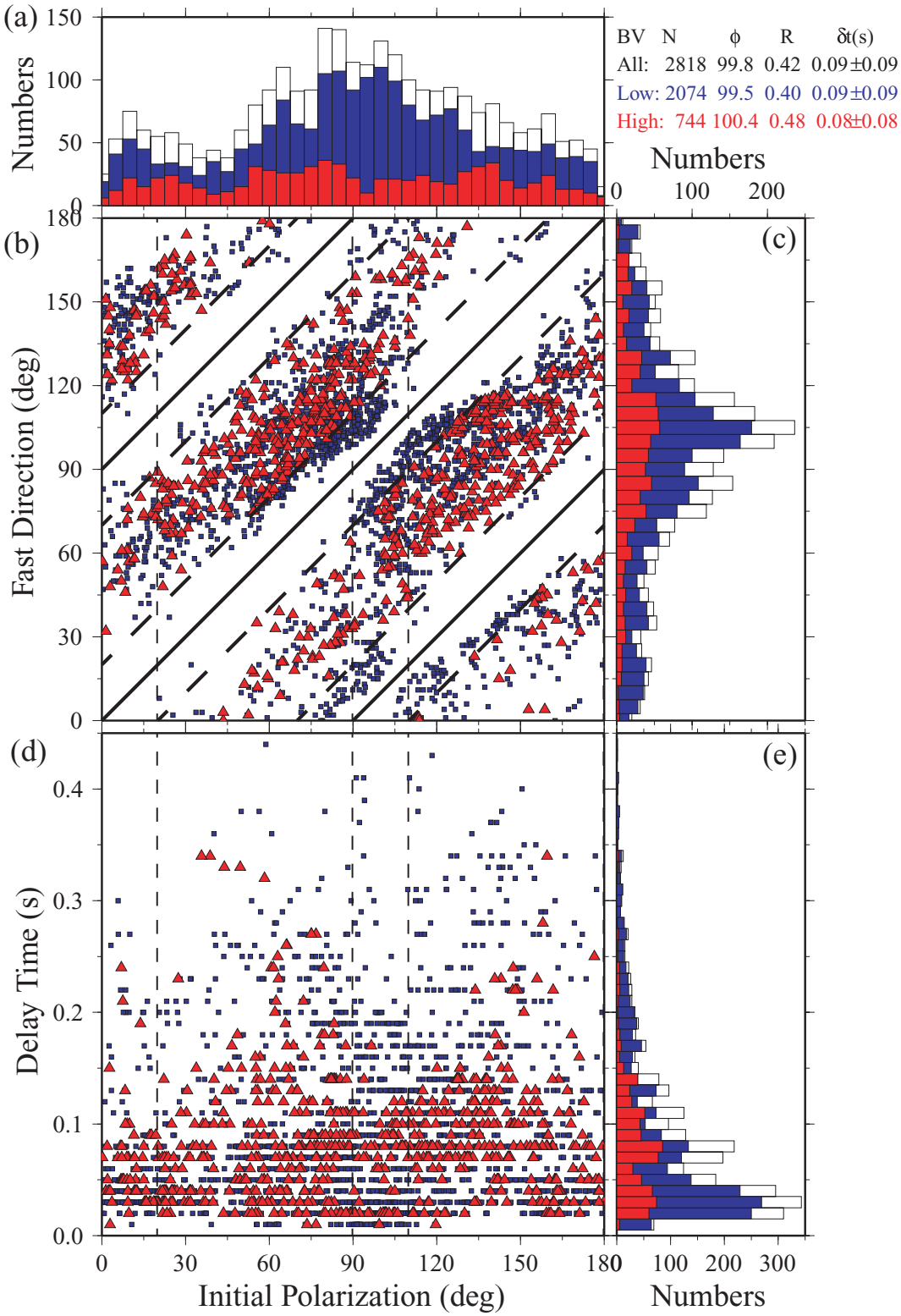

Figure 5. (a) Histograms of initial polarization for all measurements at station BV (unfilled bars) and results with low (blue) and high (red) quality. The total number of measurements N, average fast direction ϕ, mean resultant length R and average and standard deviation of δt for each category are shown at the top right corner. (b) Plot of fast direction ϕ versus initial polarization α for different qualities of measurements. The solid thick lines mark the relation $\phi = \alpha \pm 90^\circ$. The thick dashed lines mark the relations $20^\circ \leq |\phi - \alpha| \leq 70^\circ$ that we use to reject possible null measurements. The thin vertical dashed lines denote the region of values that would be discarded using the uniform rejection criterion of Cochran *et al.* (2003). Other symbols are the same as in Fig. 4. (c) Histograms of the fast direction ϕ. (d) Plot of the delay times δt versus initial polarization α. (e) Histograms of the delay time δt.

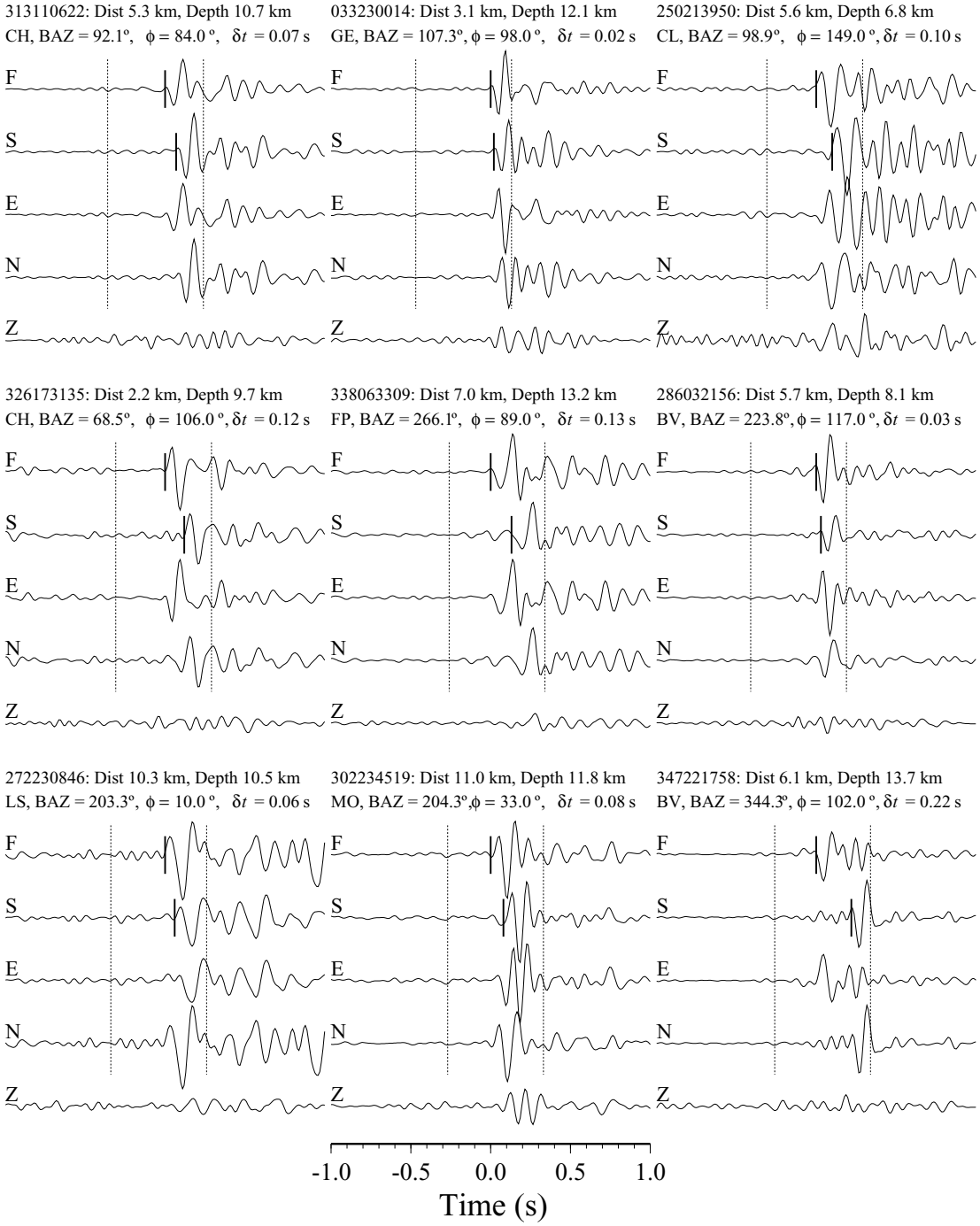

Figure 6. Examples of original and rotated waveforms that are used to determine splitting parameters of high-quality data. Horizontal seismograms are rotated into fast and slow components using the obtained ϕ and are plotted together with the original three-component waveforms. The seismograms have been low-pass filtered <15 Hz. They are plotted using a fixed amplitude scale in each panel and are aligned with *S* arrivals at 0 s. The dashed lines indicate the start and end of the time windows obtained automatically using the sliding window technique. The short vertical bars indicate the fast and slow shear wave arrivals. The event ID, epicentre distance (Dist), focal depth, station name, backazimuth (BAZ), obtained fast direction ϕ and delay time δt are shown at the top of each panel. The epicentres of the events are shown in Fig. 1(b). Events 338063309 and 033230014 are also marked on a vertical cross-section in Fig. 11, and events 281221102 and 286032156 are marked on a map view and a vertical cross-section in Fig. 17.

Prieta segment of the San Andreas fault (Zhang & Schwartz 1994), in southern Hawaii (Munson *et al.* 1995), along the rupture zones of the 1999 Hector Mine earthquake (Cochran *et al.* 2003) and in the aftershock region of the 1999 Chi-Chi, Taiwan, earthquake (Liu *et al.* 2004).

Fig. 16 gives a summary of the average δt measurements. The standard deviations are close to 0.05 s, but it is still possible to discern several important features. Earthquakes and stations that are close to the FZ have larger average δt than results associated with other source–receiver combinations of the results. The smallest average δt values are obtained when both the earthquakes and stations are outside the FZ. The FZ station BV observes one of the largest δt differences for earthquakes that are inside and outside the FZ. Fig. 17 shows splitting measurements at station BV

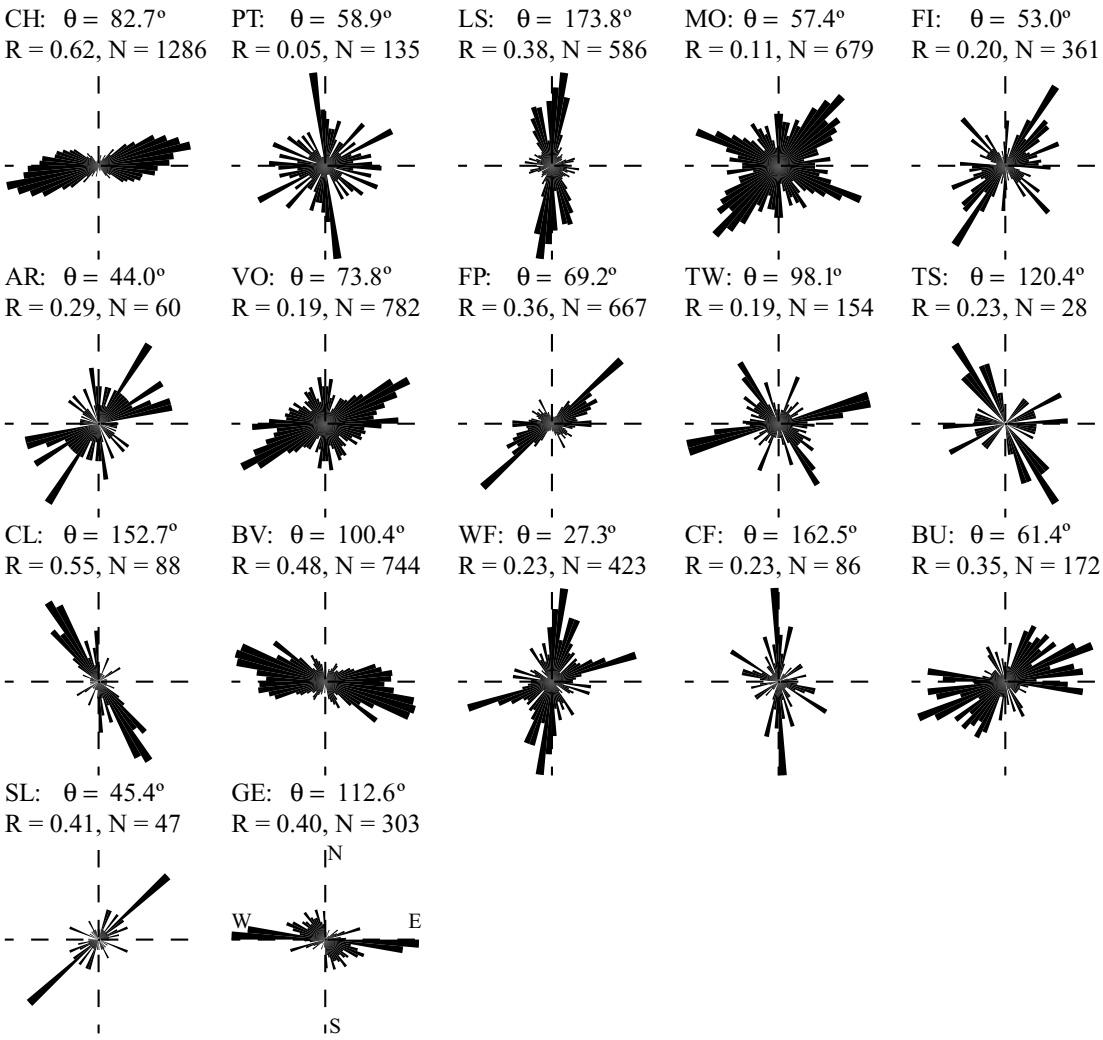

Figure 7. Rose diagrams of the fast directions ϕ at all 17 stations. The average fast direction θ, mean resultant length R and total number of measurements N at each station are shown on top of each diagram. The first 12 stations are within or close to the FZ and the other 5 are clearly outside.

on map and cross-section views. For ray paths near the ∼65° north-dipping fault, the δt values are much larger than those from the south side of the fault. These observations indicate significant damage intensity (or crack density) in the dipping rupture zone below station BV.

Although individual measurements of δt range from 0.0 to 0.3 s, the average δt for ray paths in Fig. 16 inside the FZ is approximately 0.08 ± 0.05 s for approximately 3200 measurements. The associated apparent crack density e can be estimated using $e = \beta(\delta t/L)$, where β, δt and L are the shear wave velocity of the uncracked medium, observed anisotropy delay time and propagation length in the anisotropic medium, respectively (Hudson 1981; O'Connell & Budiansky 1974). The average value of the hypocentral distances for the ∼3200 measurements is ∼13 km. Assuming that $L \sim 13$ km (i.e. that entire distance) and using $\beta = 3.2$ km s^{-1} based on the velocity model of Ben-Zion *et al.* (2003) for the material outside the fault together with our measured $\delta t \approx 0.08$ s, gives $e \approx 2$ per cent. (A similar value can be obtained by dividing the measured δt with the observed ∼4.2 s average shear wave travel time of the ∼3200 measurements.) However, this value is a lower limit of the crack density because the anisotropy in this area is confined primarily to the top 3–4 km (Figs 12–15). If we use $L = 3.5$ km for the average propagation distance inside the anisotropic medium, the apparent crack density is $e \approx 7.3$ per cent. This value is close to the 10 per cent limit of Hudson (1981), suggesting that the top 3–4 km of the Karadere–Düzce branch of the NAF is highly fractured. The ∼7 per cent estimated crack density is similar to values measured near the San Andreas fault at Parkfield (Daley & McEvilly 1990) and a normal fault near Oroville, California (Leary *et al.* 1987), while being somewhat higher than the 5 per cent value measured at the Hector Mine rupture zone (Cochran *et al.* 2003). We also note that 7 per cent is lower than inferred crack density at volcanic or geothermal regions, such as the Long Valley caldera in California (Savage *et al.* 1990), southern Hawaii (Munson *et al.* 1995) and the Cerro Prieto geothermal field in the Mexicali valley, Mexico (González & Munguía 2003).

5 DISCUSSION

We analyse crustal anisotropy using shear wave splitting measurements from a large seismic data set recorded along the Karadere–Düzce branch of the NAF in the 6 months after the 1999 İzmit earthquake (Fig. 1). We apply the Silver & Chan (1991) technique to determine splitting parameters of approximately 22 000 records within the shear wave window (Fig. 2). The time window associated with each measurement is automatically determined by a sliding

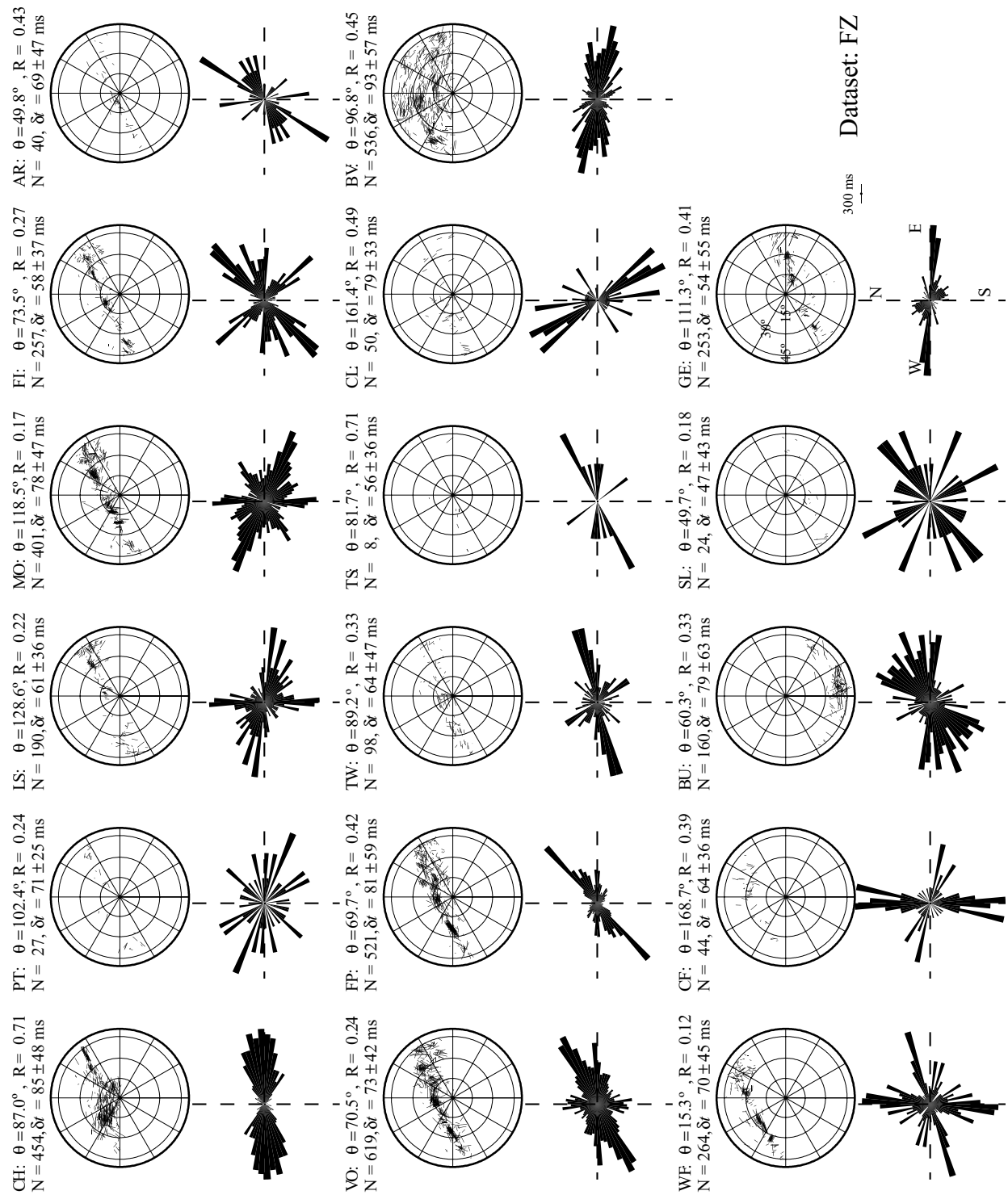

Figure 8. Rose diagrams of ϕ and equal area plots of splitting parameters (bars) at 17 stations for earthquakes belonging to the FZ group. Bars in the equal area plot are oriented parallel to ϕ and scaled by the delay time δt. The average fast direction θ, R, average and standard deviation of δt and total number of events N are marked on top of each equal area plot. The first 12 stations are within or close to the FZ and the other 5 are clearly outside.

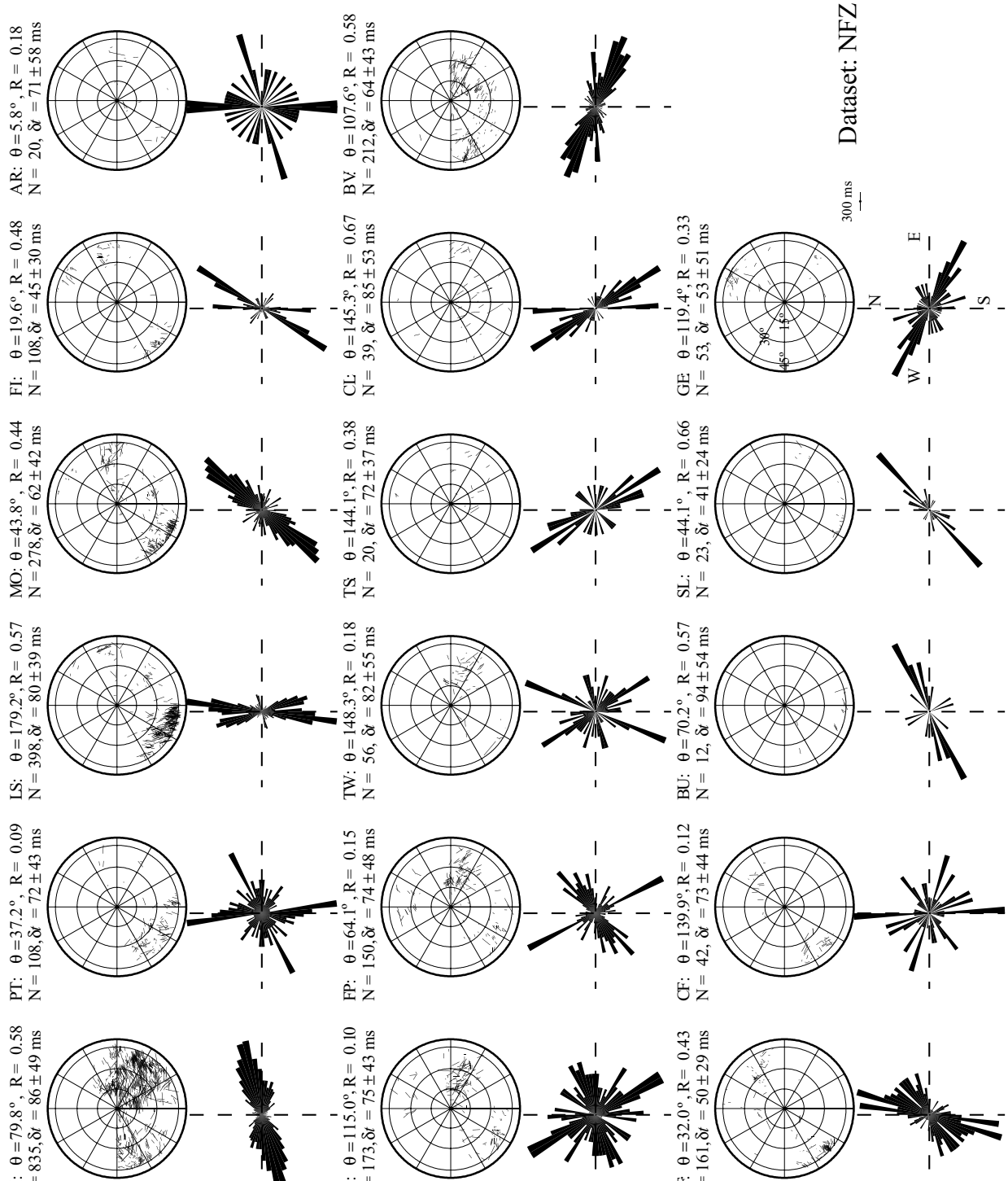

Figure 9. Rose diagrams of ϕ and equal area plots of splitting parameters (bars) at 17 stations for earthquakes belonging to the NFZ group. Other symbols are the same as in Fig. 8.

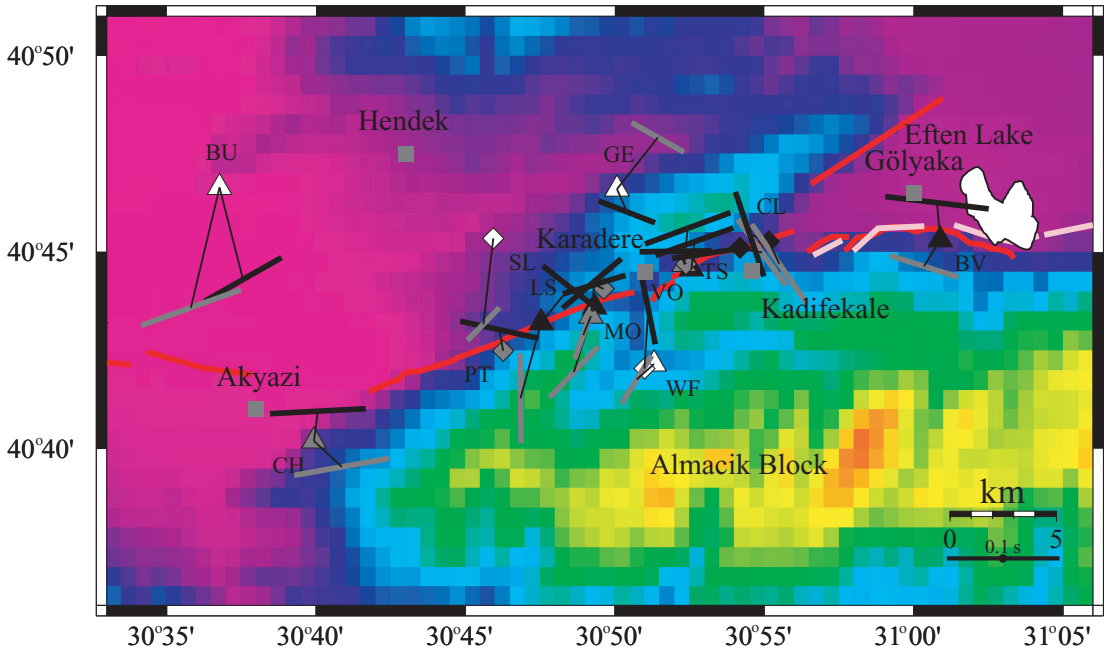

Figure 10. A summary plot of average splitting parameters (bars) in our study area. The bars are oriented parallel to the average fast direction ϕ and scaled by the average delay time δt. Dark and grey shadings of the bars denote results from earthquakes belonging to the FZ and NFZ groups, respectively. The centre of each bar is plotted at the middle point between the corresponding station and the centroid of the earthquake epicentres. The thin line connects the centre of the each bar to its corresponding station. Only average results with at least five measurements and mean resultant length of at least 0.2 are shown. The background colours denote topography with purple to blue being low and green to yellow being high. The surface ruptures of the İzmit and Düzce earthquakes are indicated with thick red and light pink lines, respectively. Other symbols and notations are the same as in Fig. 1.

window method (Fig. 3). Based on 10 objective criteria, a quality of high or low is assigned to each measurement (Figs 4 and 5). Using the high-quality data set, we find clear spatial variations of crustal anisotropy in our study area (Figs 6–11). The average fast directions θ at most FZ stations for ray paths inside the FZ are parallel to and change with the direction of the fault strike nearby. The average delay times δt for ray paths that propagate inside the FZ are larger than for other paths (Figs 16 and 17). These results suggest fault-parallel cracks or shear fabric as possible sources for the observed anisotropy near the fault. However, FZ stations TS and CL that are near geometrical complexities have θ of approximately NW–SE, which is almost perpendicular to the local fault strike (Fig. 10). Some FZ stations (e.g. LS, MO) have either scattered or bimodal fast directions. The observations indicate collectively significant variations of FZ properties along the fault strike.

The average fast direction θ from ray paths that propagate inside the Almacik block is between 0° and 40° (Fig. 10). The observed anisotropy within the block is most likely caused by lithologic properties such as foliation, bedding, or aligned minerals. The average fast direction at station GE off the fault is close to the regional σ_H direction of approximately NW–SE. However, stations BU and SL have fast directions that are NE–SW, almost perpendicular to σ_H. These observations indicate again strong spatial variations of anisotropy. Our results suggest that several different mechanisms contribute to the observed anisotropy in this area. Most stations do not show a clear increase of δt with increasing depth and hypocentral distance, indicating that the anisotropy is confined primarily to the top 3–4 km of the crust (Figs 12–15).

Ben-Zion *et al.* (2003) performed a systematic analysis of seismic FZ trapped waves using the same data set and found that the trapping of seismic energy in the Karadere–Düzce fault is generated by ∼100-m-wide FZ layer that extends to a depth of ∼3–4 km. Here, we find that fault-parallel ϕ exists at stations that are within several hundred metres on either side of the surface rupture (e.g. stations FI and FP), but not at stations that are several kilometres away (e.g. station GE). This suggests that a high density of microcracks exists in a broader region (e.g. kilometres wide) than the ∼100-m-wide seismic trapping layers (Ben-Zion *et al.* 2003). A similar structure with a broad damage zone around a more intense narrower FZ layer was mapped in the field (Faulkner *et al.* 2003) at the Carboneras fault, Spain. Fialko *et al.* (2002) observed from InSAR data damage zones that are several kilometres wide around faults in the eastern California shear zone. Various gravity, electromagnetic and seismic imaging studies around large faults also indicate a few kilometre wide damage zones (Ben-Zion & Sammis 2003 and references therein). Most of these studies do not resolve the depth extent of the broad damage zones, but they are likely to be confined primarily to the top few kilometres of the crust, as found here and in the studies of Savage *et al.* (1990), Zhang & Schwartz (1994), Munson *et al.* (1995), Cochran *et al.* (2003) and Liu *et al.* (2004). We note that a depth of approximately 3 km corresponds to the inferred transition (Blanpied *et al.* 1991) from an aseismic velocity-strengthening behavior to a seismic velocity-weakening regime of rate- and state-dependent friction (e.g. Dieterich 1979, 1981; Marone & Scholz 1988). This provides a possible explanation for a change in the FZ structure from a broadly deforming, mechanically passive, stable shallow structure in the top 3 km, to a considerably narrower seismic structure in the deeper section.

The inferred average crack density for ray paths with effective propagation distance of 3–4 km in the damaged shallow portion of the FZ is approximately 7 per cent. It is possible that some crack-induced anisotropy exists at larger depth, as was found for example in the KTB deep drill hole in Germany (e.g. Rabbel 1994; Bokelmann & Harjes 2000). However, as a result of the increasing

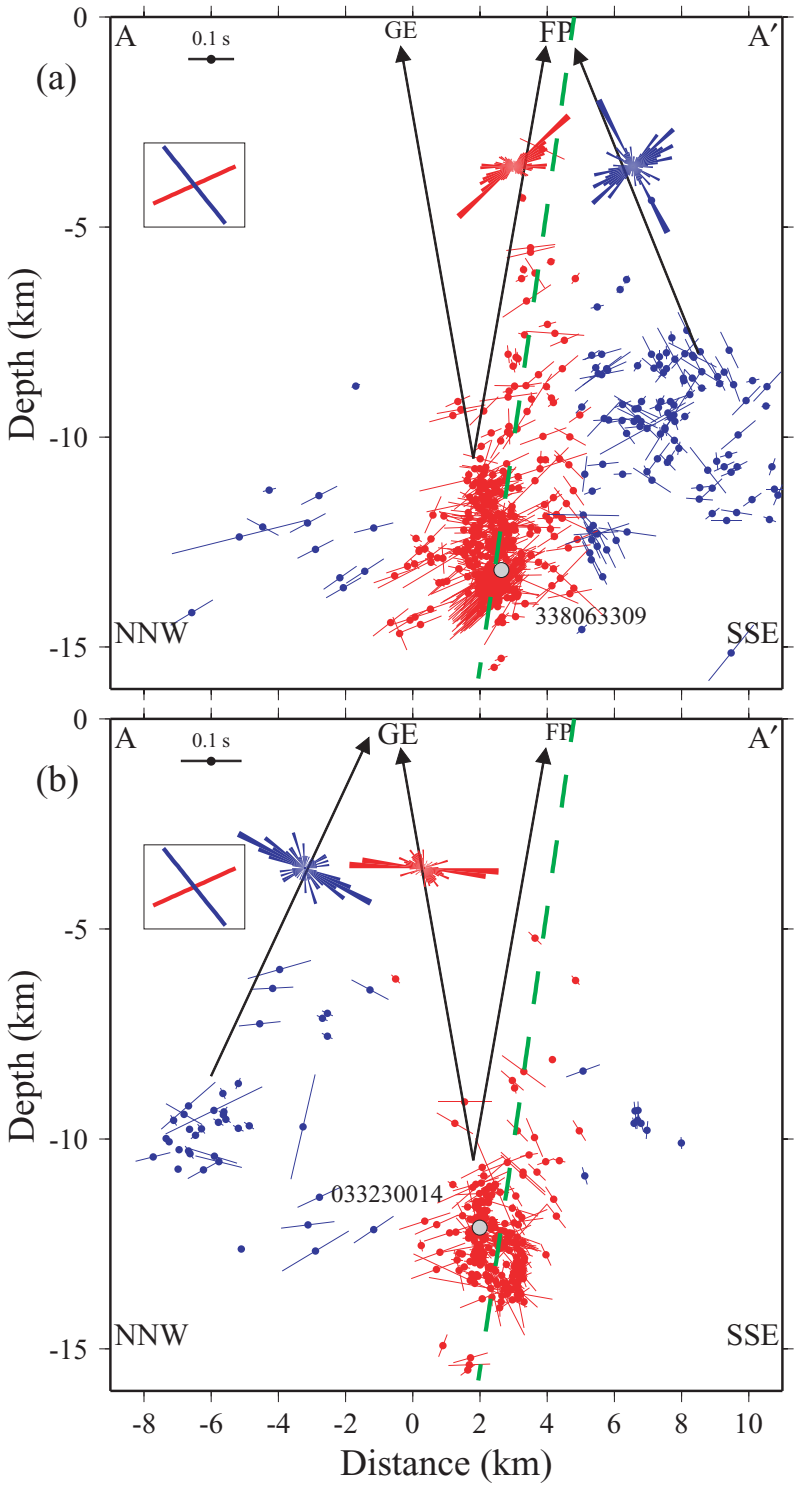

Figure 11. (a) Splitting parameters (bars) superimposed on the hypocentral locations within the shear wave window of the FZ station FP and projected along the cross-section AA′ in Fig. 1(b). The bars are oriented parallel to the fast polarization direction ϕ and scaled by the delay time δt. [Note that the zones producing the anisotropy are likely to be considerably shallower (Figs 12–15) than the earthquakes where the symbols are located.] Red and blue colours denote results from earthquakes belonging to FZ and NFZ groups, respectively. The green dashed line indicates the ∼80° north-dipping fault along the Karadere segment that ruptured during the İzmit earthquake. The long lines with arrows show schematic straight-line ray paths for different source–station configurations and the rose diagrams summarize the results of fast polarization directions of different earthquake groups. The regional maximum horizontal compressive stress direction σ_H and the direction of fault strike nearby are shown in the inset by blue and red lines, respectively. Waveforms generated by the event marked by the grey circle are shown in Fig. 6. (b) Splitting parameters (bars) superimposed on the hypocentral locations within the shear wave window of the regional station GE and projected along the cross-section AA′ in Fig. 1(b). Other symbols and notations are the same as in (a).

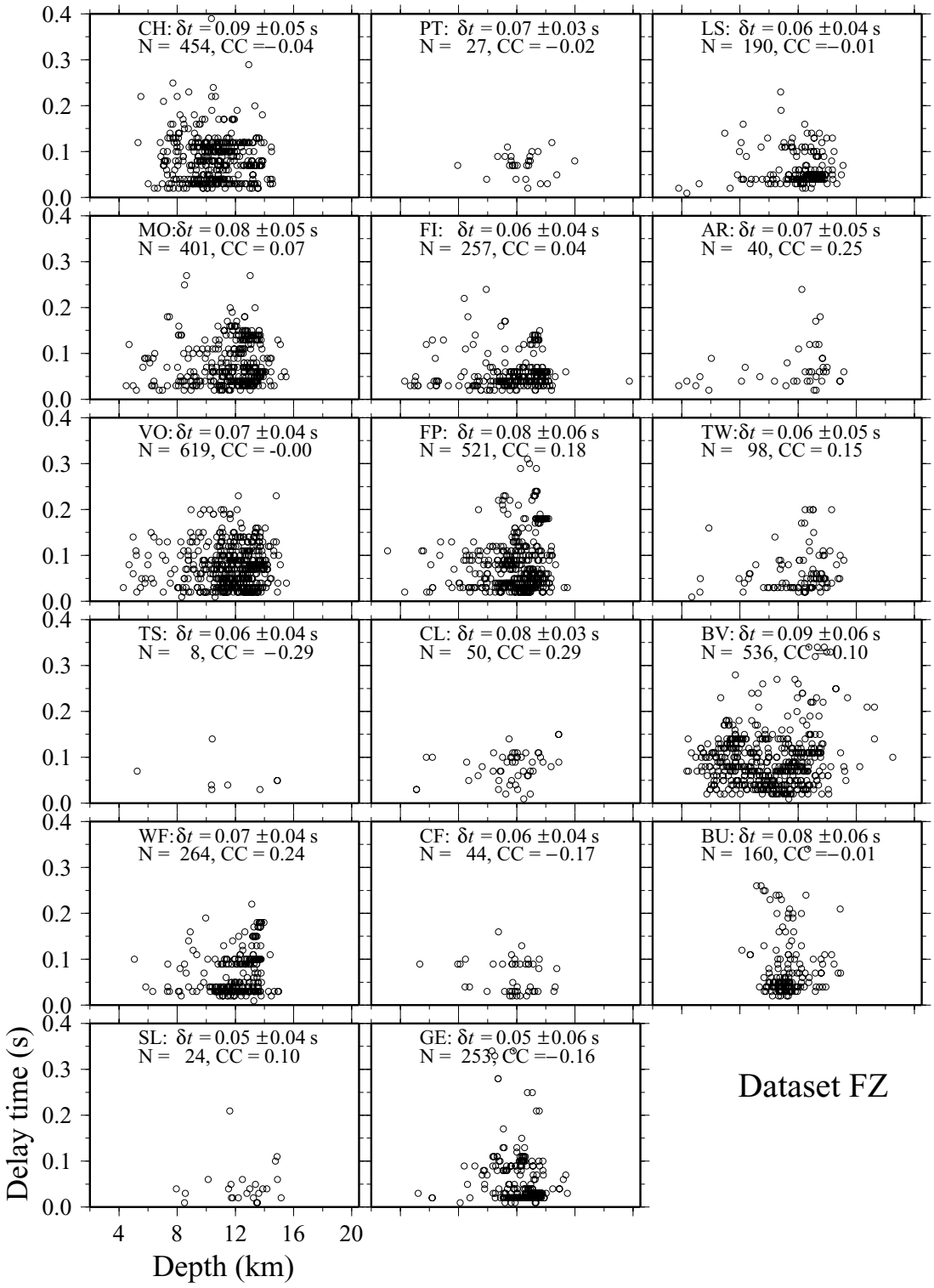

Figure 12. Delay time versus depth at all stations for earthquakes that belong to the FZ group. The station name, average and standard deviation of δt, total number of events (N), and correlation coefficients (CC) between δt and depth are marked on top of each panel.

confining pressure, the crack density should decrease in general with increasing depth (e.g. Boness & Zoback 2004; Liu *et al.* 2004). As discussed above, the crack density is also likely to have a strong reduction at the transition from a velocity-strengthening to a velocity-weakening frictional regime. Because the observed anisotropy is dominated by the shallow crust, the results do not provide in general information on properties of the FZ structure at seismogenic depth where the bulk of seismic energy is stored and released. A similar conclusion holds for analysis of FZ trapped waves (Ben-Zion *et al.* 2003; Peng *et al.* 2003).

There has been considerable controversy over the possibility of using temporal variations of crustal anisotropy to monitor

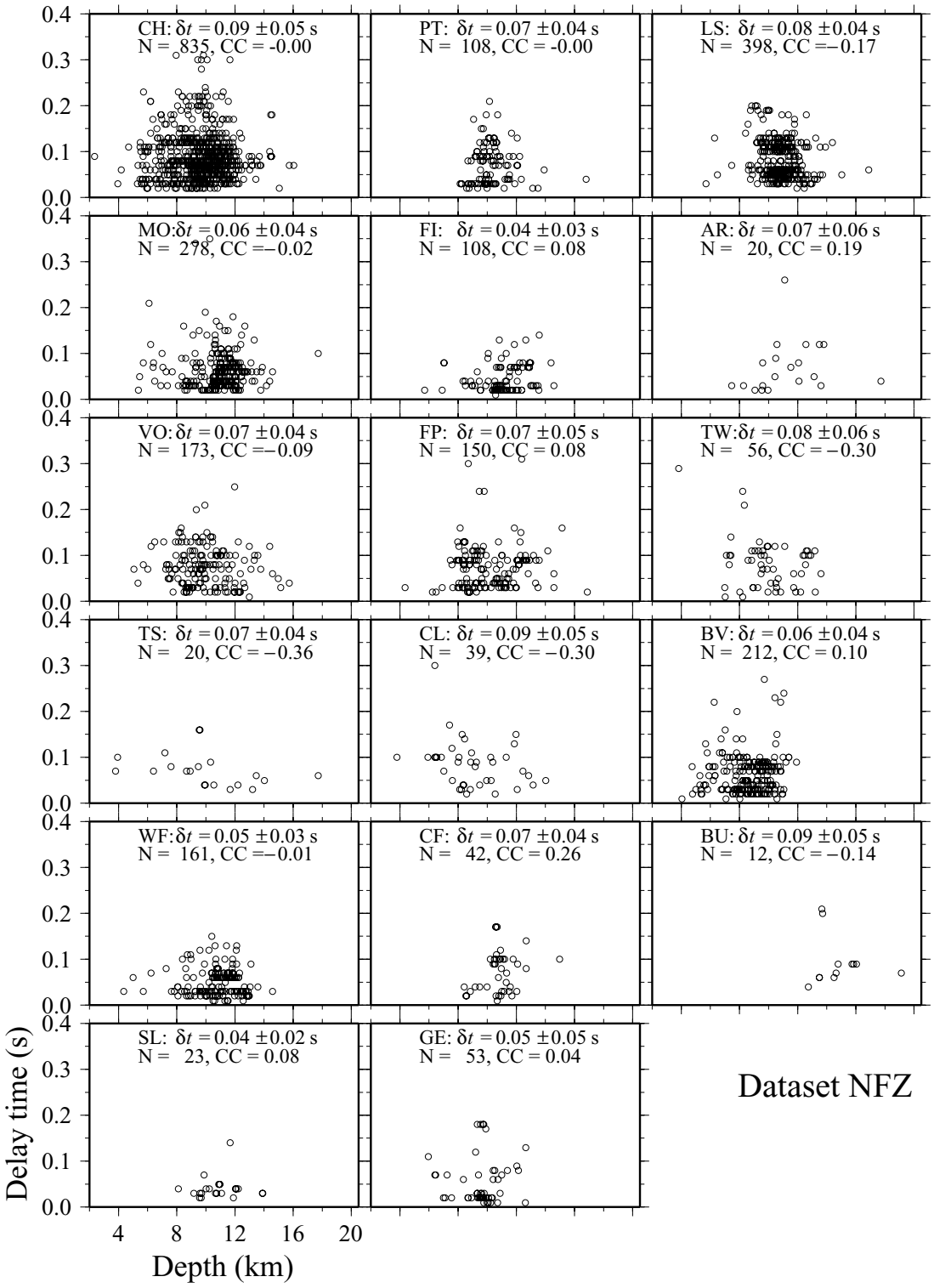

Figure 13. Delay time versus depth at all stations for earthquakes that belong to the NFZ group. Other symbols and notations are the same as in Fig. 12.

precursory stress changes before major earthquakes (e.g. Aster *et al.* 1990; Crampin *et al.* 1990; Aster *et al.* 1991; Crampin *et al.* 1991; Munson *et al.* 1995; Crampin *et al.* 1999). Recent studies also claim that temporal changes of crustal anisotropy can be used to monitor coseismic stress changes (Saiga *et al.* 2003), post-seismic fault healing (Tadokoro & Ando 2002; Tadokoro *et al.* 2002) and volcano eruptions (Miller & Savage 2001; Gerst 2003). In complex regions, like the one examined here, where several different mechanisms may contribute to the observed anisotropy, temporal variations, even if such exist, may be contaminated by variations of ray paths as a result of the changing seismicity.

The present paper was focused on the development of an automatic and objective shear wave splitting methodology that can be applied to a large data set and deriving general spatial

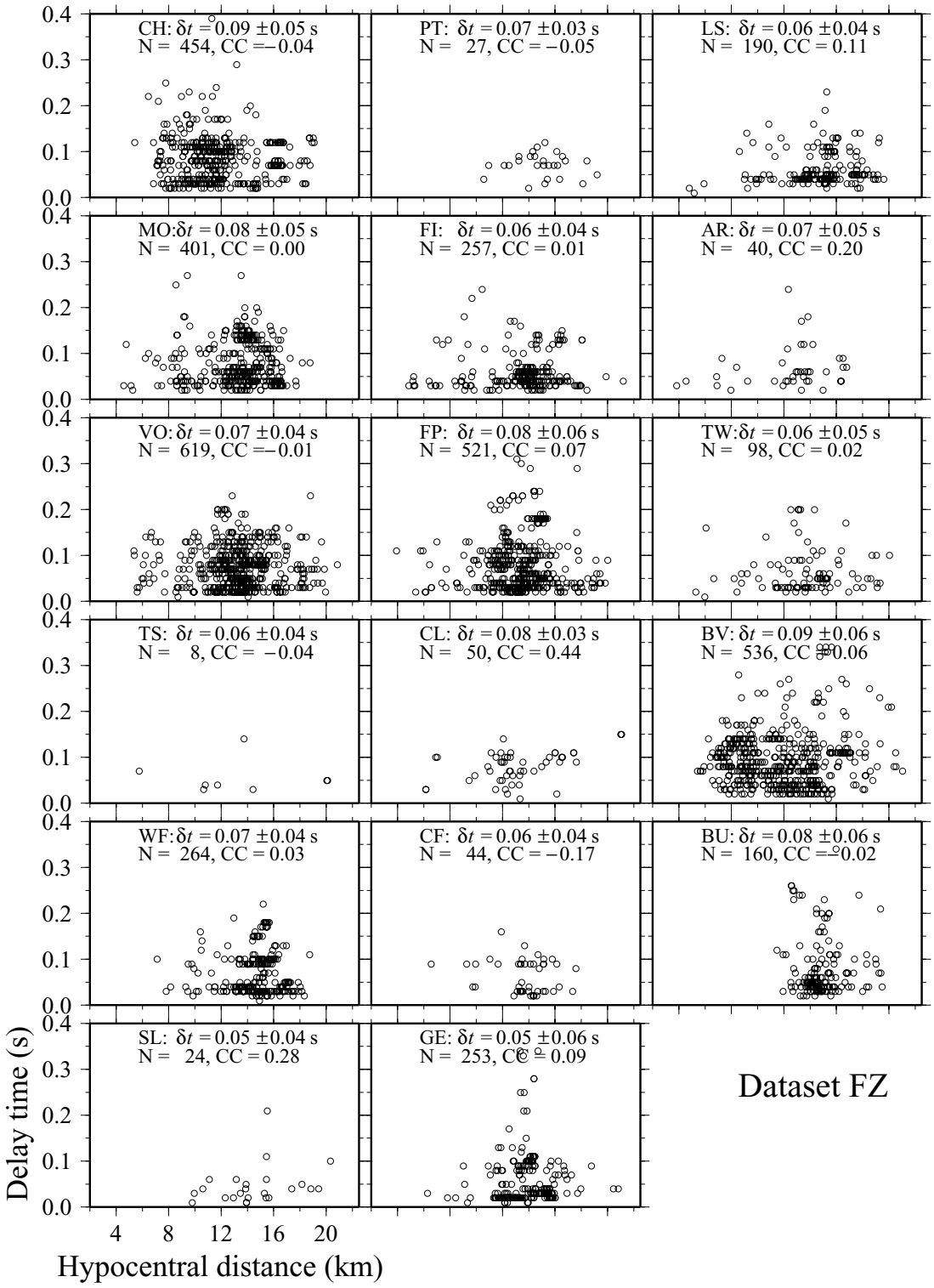

Figure 14. Delay time versus hypocentral distance at all stations for earthquakes that belong to the FZ group. Other symbols and notations are the same as in Fig. 12.

properties of the crustal anisotropy in our study area. Detailed space–time variations of crustal anisotropy around Karadere–Düzce branch of the NAF using similar earthquake clusters are discussed in a follow up paper (Peng & Ben-Zion 2004). The results from the similar earthquake clusters show, in agreement with the present study, clear large spatial variations of crustal anisotropy. Splitting parameters measured from similar earthquake clusters indicate at most 2 per cent coseismic changes of delay times associated with the occurrence of the Düzce main shock. Small coseismic and post-seismic changes of seismic properties are also revealed by analysis of relative travel times and evolving decorrelation of *P*- and *S*-coda waves of similar earthquake clusters. The

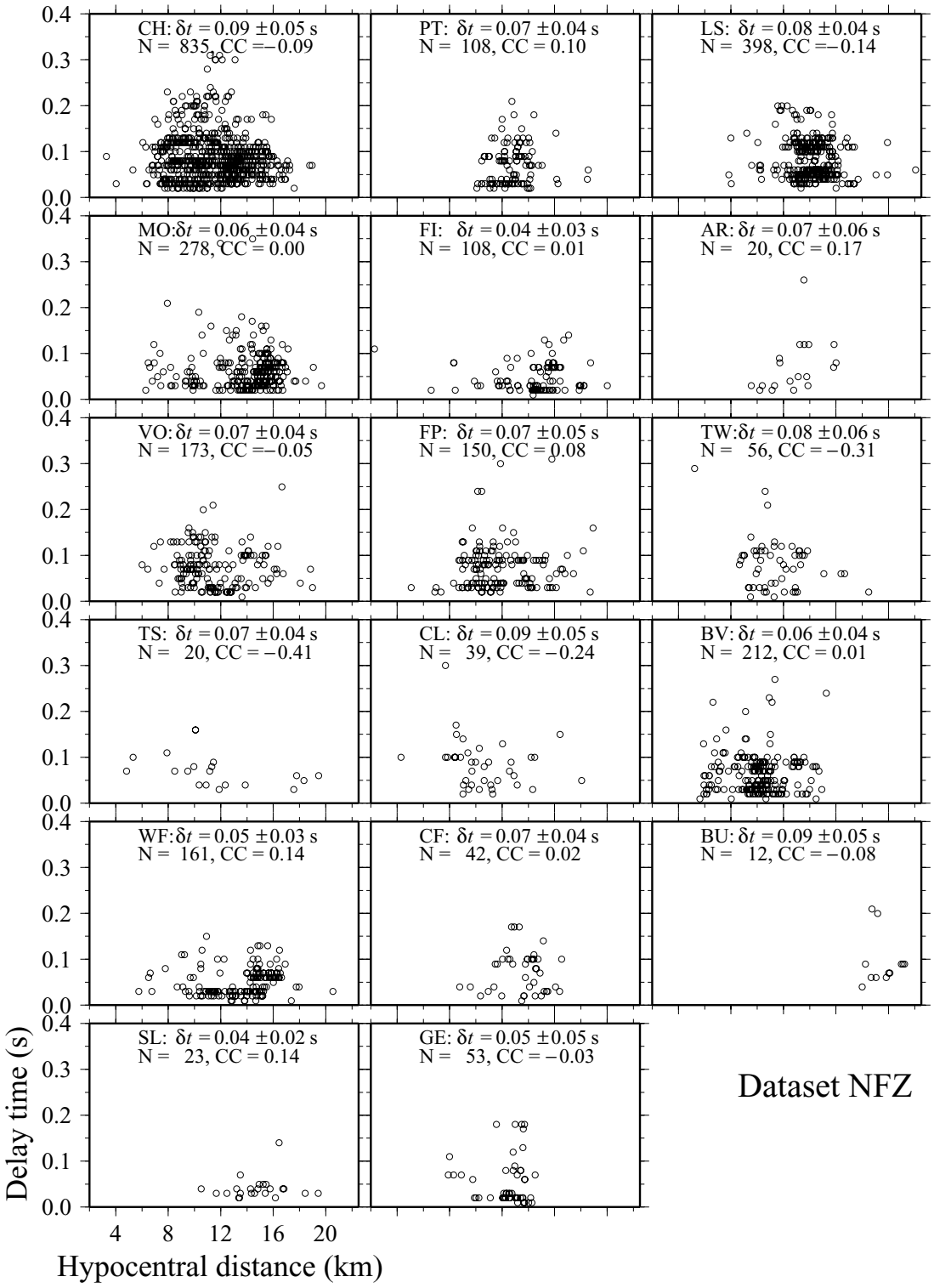

Figure 15. Delay time versus hypocentral distance at all stations for earthquakes that belong to the NFZ group. Other symbols and notations are the same as in Fig. 12.

results do not show systematic precursory changes before the Düzce main shock.

ACKNOWLEDGMENTS

The authors thank John Armbruster, David Okaya, Naside Ozer and Nano Seeber for essential help with the fieldwork and PASSCAL for providing the equipment and technical support for the experiment. The authors also thank Paul Silver for sharing his shear wave splitting code and Elizabeth Cochran, Yunfeng Liu, David Okaya, Leon Teng and John Vidale for useful discussions. The manuscript benefited from comments by the Editor Russ Evans and two anonymous reviewers. All figures in the paper are generated using GMT (Wessel & Smith 1998). The

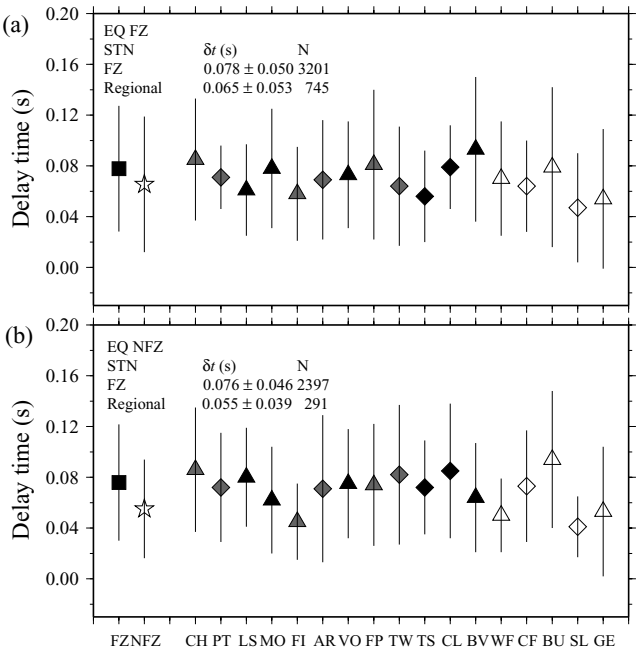

Figure 16. Average delay times δt for earthquakes that are (a) located close or near the FZ and (b) outside the FZ (regional). Triangles and diamonds denote the average δt for stations deployed for approximately 6 months and 2 weeks, respectively. Values for stations within, near and outside the FZ are shaded with dark, grey and white colours, respectively. Squares and stars mark the average δt values for all 12 stations near the FZ and those for the 5 regional stations, respectively. The vertical line at each point is the standard deviation of the result. The average and standard deviation of δt and total number of events N for FZ and regional stations are marked on the top of each panel.

study was supported by the National Science Foundation (grant EAR0003401).

REFERENCES

Akyüz, H.S., Barka, A., Altunel, E., Hartleb, R. & Sunal, G., 2000. Field observations and slip distribution of the November 12, 1999 Düzce earthquake (M = 7.1), Bolu, Turkey, in *The 1999 İzmit and Düzce Earthquakes: preliminary results,* pp.63–70, eds Barka *et al.,* Istanbul Technical University, Istanbul.

Aster, R.C., Shearer, P.M. & Berger, J., 1990. Quantitative measurements of shear wave polarizations at the Anza seismic network, southern California: Implications for shear wave splitting and earthquake prediction, *J. geophys. Res.,* **95,** 12 449–12 473.

Aster, R.C., Shearer, P.M. & Berger, J., 1991. Comments on Quantitative measurements of shear wave polarization at the Anza seismic network, Southern California: Implications for shear wave splitting and earthquake prediction, *J. geophys. Res.,* **96,** 6415–6419.

Aster, R.C. & Shearer, P.M., 1992. Initial shear wave particle motions and stress constraints at the Anza Seismic Network, *Geophys. J. Int.,* **108,** 740–748.

Barka, A., 1996. Slip distribution along the North Anatolian fault associated with large earthquakes of the period 1939 to 1967, *Bull. seism. Soc. Am.*, **59,** 521–589.

Barka, A. *et al.*, 2002. The Surface Rupture and Slip Distribution of the 17 August 1999 İzmit Earthquake (M 7.4), North Anatolian Fault, *Bull. seism. Soc. Am.,* **92,** 43–60.

Ben-Zion, Y. *et al.*, 2003. A shallow fault zone structure illuminated by trapped waves in the Karadere–Düzce branch of the North Anatolian Fault, western Turkey, *Geophys. J. Int.,* **152,** 699–717.

Ben-Zion, Y. & Sammis, C.G., 2003. Characterization of fault zones, *Pure appl. Geophys.,* **160,** 677–715.

Bellier, O., Over, S., Poisson, A. & Andrieux, J., 1997. Recent temporal change in the stress state and modern stress field along the North Anatolian fault zone (Turkey), *Geophys. J. Int.,* **131,** 61–86.

Blanpied, M.L., Lockner, D.A. & Byerlee, J.D., 1991. Fault stability inferred from granite sliding experiments at hydrothermal conditions, *Geophys. Res. Lett.,* **18(4),** 609–612.

Blenkinsop, T.G., 1990. Correlation of paleotectonic fracture and microfracture orientations in cores with seismic anisotropy at Cajon Pass drill hole, southern California, *J. geophys. Res.,* **95,** 11 143–11 150.

Bokelmann, G.H.R. & Harjes, H.P., 2000. Evidence for temporal variation of seismic velocity within the upper continental crust, *J. geophys. Res.,* **105,** 23 879–23 894.

Boness, N. & Zoback, M.D., 2004. Stress-induced seismic velocity anisotropy and physical properties in the SAFOD pilot hole in Parkfield, CA, *Geophys. Res. Lett.,* **31,** L15S17, doi:10.1029/2004GL019020.

Booth, D.C. & Crampin, S., 1985. Shear-wave polarizations on a curved wavefront at an isotropic free-surface, *Geophys. J. R. astron. Soc.*, **83,** 31–45.

Bouin, M.P., Tellez, J. & Bernard, P., 1996. Seismic anisotropy around the Gulf of Corinth, Greece, deduced from three-component seismograms of local earthquakes and its relationship with crustal strain, *J. geophys. Res.,* **101,** 5795–5811.

Brocher, T.M. & Christensen, N.I., 1990. Seismic anisotropy due to preferred mineral orientation observed in shallow crustal rocks in southern Alaska, *Geology,* **18,** 737–740.

Cochran, E.S., Vidale, J.E. & Li, Y.-G., 2003. Near-fault anisotropy following the Hector Mine earthquake, *J. geophys. Res.,* **108**(B9), 2436, doi:10.1029/2002JB002352.

Crampin, S., 1978. Seismic wave propagation through a cracked solid: polarization as a possible dilatancy diagnostic, *Geophys. J. R. astr. Soc.,* **53,** 467–496.

Crampin, S., 1981. A review of wave motion in anisotropic and cracked elastic-media, *Wave Motion,* **3,** 343–391.

Crampin, S., 1987. Geological and industrial implications of extensive-dilatancy anisotropy, *Nature,* **328,** 491–496.

Crampin, S., 1994. The fracture criticality of crustal rocks. *Geophys. J. Int.,* **118,** 428–438.

Crampin, S., Booth, D.C., Evans, R., Peacock, S. & Fletcher, J.B., 1990. Change in shear wave splitting at Anza near the time of the North Palm Springs earthquake, *J. geophys. Res.,* **95,** 11 197–11 212.

Crampin, S., Booth, D.C., Evans, R., Peacock, S. & Fletcher, J.B., 1991. Comment on 'Quantitative measurements of shear wave polarizations at the Anza seismic network, Southern California: Implications for shear wave splitting and earthquake predication' by R.C. Aster, P. M. Shearer, and J. Berger, *J. geophys. Res.,* **96,** 6403–6414.

Crampin, S., Volti, T. & Stefánsson, R., 1999. A successfully stress-forecast earthquake, *Geophys. J. Int.,* **138,** F1–F5.

Crampin, S., Peacock, S., Gao, Y. & Chastin, S., 2004. The scatter of time-delays in shear-wave splitting above small earthquakes, *Geophys. J. Int.,* **156,** 39–44.

Daley, T.M. & McEvilly, T.V., 1990. Shear wave anisotropy in the Parkfield Varian Well VSP, *Bull. seism. Soc. Am.,* **80**(4), 857–869.

Davis, J. C., 1986. *Statistics and Data Analysis in Geology,* John Wiley, Hoboken, NJ, USA, p. 646.

Dieterich, J.H., 1979. Modeling of rock friction 1. Experimental results and constitutive equations, *J. geophys. Res.,* **84,** 2161–2168.

Dieterich, J.H., 1981. Constitutive properties of faults with simulated gouge, *Am. geophys. Un. Monogr.,* **24,** 103–120.

Faulkner, D.R., Lewis, A.C. & Rutter, E.H., 2003. On the internal structure and mechanics of large strike-slip fault zones: field observations of the Carboneras fault in southeastern Spain, *Tectonophysics,* **367,** 235–251.

Fialko, Y., Sandwell, D., Agnew, D., Simons, M., Shearer, P. & Minster, B., 2002. Deformation on nearby faults induced by the 1999 Hector Mine earthquake, *Science*, **297,** 1858–1862.

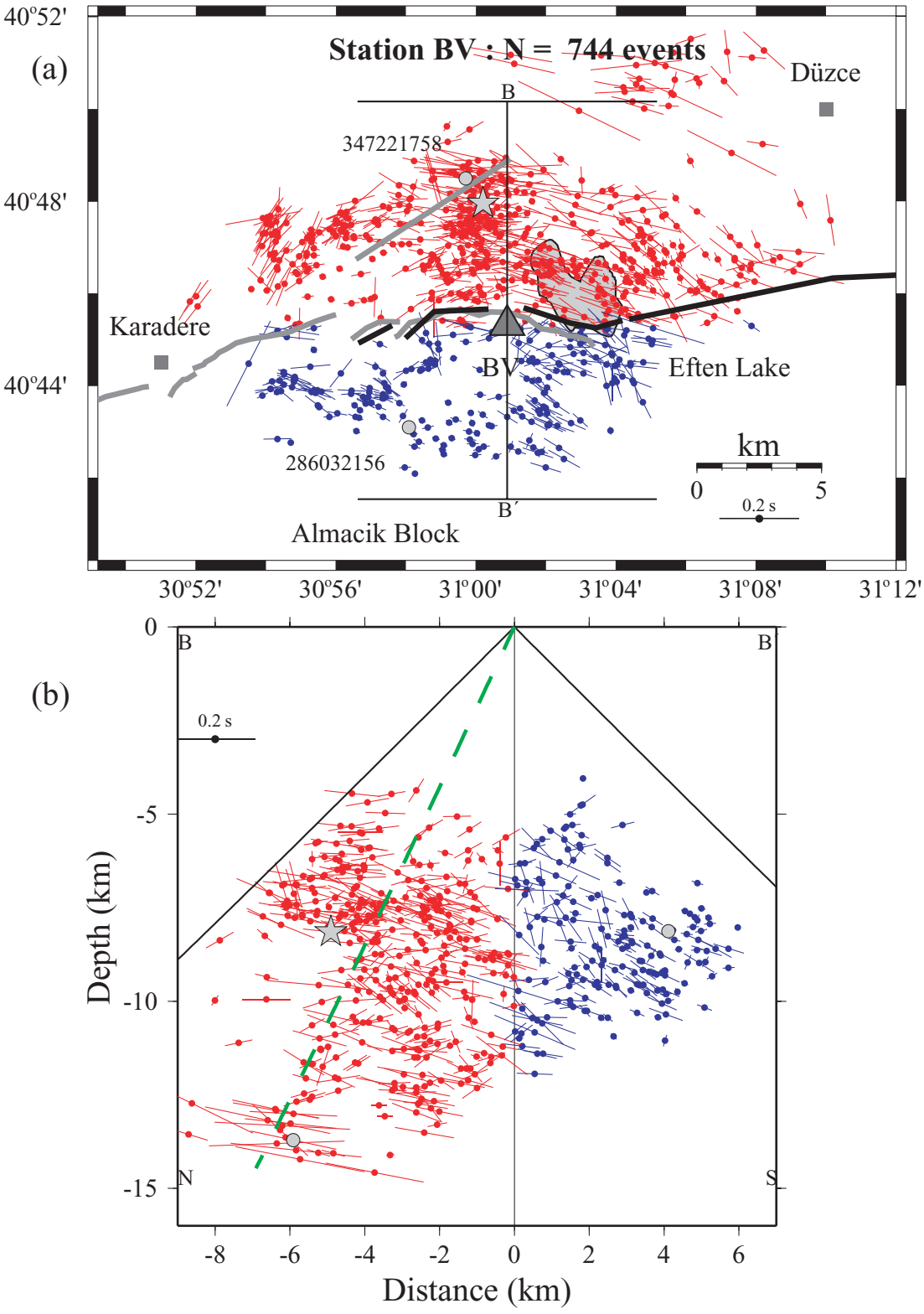

Figure 17. (a) Splitting parameters (bars) for station BV superimposed on the hypocentral locations within the shear wave window. The bars are oriented parallel to the fast polarization direction ϕ and scaled by the delay time δt. [Note that the zones producing the anisotropy are likely to be considerably shallower (Figs 12–15) than the earthquakes where the symbols are located.] Red and blue colours denote results from earthquakes belonging to FZ and NFZ groups, respectively. Waveforms generated by the event marked by the star and the two events marked by the circles are shown in Figs 2 and 6, respectively. (b) Splitting parameters superimposed on the hypocentral locations projected along the cross-section BB′ in (a) and Fig. 1(b). The dark lines denote the straight-line 45° angles that are used as the shear wave window. The green dashed line indicates the ∼ 65° north-dipping fault that ruptured during the Düzce earthquake. Other symbols and notations are the same as in (a).

Gamar, F. & Bernard, P., 1997. Shear wave anisotropy in the Erzincan basin and its relationship with crustal strain, *J. geophys. Res.,* **102,** 20 373–20 393.

Gerst, A., 2003. Temporal changes in seismic anisotropy as a new eruption forecasting tool?, *MSc Thesis*, Victoria University of Wellington, New Zealand.

Gledhill, K.R., 1991. Evidence for shallow and pervasive seismic anisotropy in the Wellington Region, New Zealand, *J. geophys. Res.,* **96,** 21 503–21 516.

González, M. & Munguía, L., 2003. Seismic anisotropy observations in the Mexicali valley, Baja California, Mexico, *Pure appl. Geophys.,* **160,** 2257–2278.

Hartleb, R.D. *et al.*, 2002. Surface Rupture and Slip Distribution along the Karadere Segment of the 17 August 1999 İzmit and the Western Section of the 12 November 1999 Düzce, Turkey, Earthquakes, *Bull. seism. Soc. Am.,* **92(1),** 67–78.

Hudson, J.A., 1981. Wave speeds and attenuation of elastic waves in material containing cracks, *Geophys. J. R. astr. Soc.,* **64,** 133–150.

Kaneshima, S., 1990. Origin of crustal anisotropy: Shear wave splitting studies in Japan, *J. geophys. Res.,* **95,** 11 121–11 133.

Kern, H. & Wenk, H., 1990. Fabric-related velocity anisotropy and shear wave splitting in rocks from the Santa Rosa mylonite zone, California. *J. geophys. Res.,* **95,** 11 213–11 223.

Klein, W., 1978. *Hypocenter location program HYPOINVERSE*, Open File Report 78–694, US Geological Survey, Boulder, CO, USA.

Langridge, R.M., Stenner, H.D., Fumal, T.E., Christofferson, S.A., Rockwell, T.K., Hartleb, R.D., Bachhuber, J. & Barka, A.A., 2002. Geometry, Slip Distribution, and Kinematics of Surface Rupture on the Sakarya Fault Segment during the 17 August 1999 İzmit, Turkey, Earthquake, *Bull. seism. Soc. Am.,* **92**(1), 107–125.

Leary, P.C., Li, Y.G. & Aki, K., 1987. Observations and modeling of fault zone fracture anisotropy, I, P, SV, SH travel times, *Geophys. J. R. astr. Soc.,* **91,** 461–484.

Leary, P.C., Crampin, S. & McEvilly, T.V., 1990. Seismic fracture anisotropy in the Earth's crust: An overview, *J. geophys. Res.,* **95**(7), 11 105–11 114.

Li, Y.-G., Teng, T.-L. & Henyey, T.L., 1994. Shear-wave observations in the Northern Los Angeles Basin, Southern California, *Bull. Seism. Soc. Am.,* **84,** 307–323.

Liu, Y., Teng, T.-L. & Ben-Zion, Y., 2004. Systematic analysis of shear-wave splitting in the aftershock zone of the 1999 Chi-Chi earthquake: shallow crustal anisotropy and lack of precursory variations, *Bull. seism. Soc. Am.,* in press.

Lyakhovsky, V., Ben-Zion, Y. & Agnon, A., 1997. Distributed damage, faulting, and friction, *J. geophys. Res.,* **102,** 27 635–27 649.

Mardia, K.V. & Jupp, P.E., 2000. *Directional Statistics*, John Wiley, Hoboken, NJ, USA, p. 429.

Marone, C. & Scholz, C.H., 1988. The depth of seismic faulting and the upper transition from stable to unstable regimes, *Geophys. Res. Lett.,* **15,** 621–624.

Matcham, I., Savage, M.K. & Gledhill, K.R., 2000. Distribution of seismic anisotropy in the subduction zone beneath the Wellington region, New Zealand, *Geophys. J. Int.,* **140,** 1–10.

Miller, V. & Savage, M.K., 2001. Changes in seismic anisotropy after volcanic eruptions: evidence from Mount Ruapehu, *Science*, **293,** 2231–2233.

Munson, C.G., Thurber, C.H., Li, Y. & Okubo, P.G., 1995. Crustal shear wave anisotropy in southern Hawaii: Spatial and temporal analysis, *J. geophys. Res.,* **100**(B10), 20 367–20 377.

Nur, A., 1971. Effects of stress on velocity anisotropy in rocks with cracks, *J. geophys. Res.,* **76,** 2022–2034.

Nur, A. & Simmons, G., 1969. Stress-induced velocity anisotropy in rock: An experimental study, *J. geophys. Res.,* **74**(27), 6667–6674.

Nuttli, O., 1961. The effect of earth's surface on the S-wave particle motion, *Bull. seism. Soc. Am.,* **51,** 237–246.

O'Connell, R.J. & Budiansky, B., 1974. Seismic velocities in dry and saturated cracked solids, *J. geophys. Res.,* **79**(35), 5412–5426.

Peacock, S., Crampin, S. & Booth, D.C., 1988. Shear wave splitting in the Anza seismic gap, southern California: temporal variations as possible precursors, *J. geophys. Res.,* **93,** 3339–3356.

Peng, Z. & Ben-Zion, Y., 2004. Spatio-temporal variations of crustal anisotropy from similar events in aftershocks of the 1999 M7.4 İzmit and M7.1 Düzce, Turkey, earthquake sequences, *Geophys. J. Int.,* submitted.

Peng, Z., Ben-Zion, Y., Michael, A.J. & Zhu, L., 2003. Quantitative analysis of fault zone waves in the rupture zone of the Landers, 1992, California earthquake: Evidence for a shallow trapping structure, *Geophys. J. Int.,* **155,** 1021–1041.

Rabbel, W., 1994. Seismic anisotropy at the Continental Deep Drilling Site (Germany), *Tectonopysics*, **232,** 329–341.

Reilinger, R.E. *et al.*, 1997. Global Positioning System measurements of the present day crustal movements in the Arabia-Africa-Eurasia plate collision zone, *J. geophys. Res.,* **102,** 9983–9999.

Saiga, A., Hiramatsu, Y., Ooida, T. & Yamaoka, K., 2003. Spatial variation in the crustal anisotropy and its temporal variation associated with a moderate-sized earthquake in the Tokai region, central Japan, *Geophys. J. Int.,* **154,** 695–705.

Savage, M.K., 1999. Seismic anisotropy and mantle deformation: what have we learned from shear wave splitting, *Rev. Geophys.,* **37,** 65–106.

Savage, M.K., Shih, X.R., Meyer, R.P. & Aster, R.C., 1989. Shear-wave anisotropy of active tectonic regions via automated S-wave polarization analysis, *Tectonophysics*, **165,** 279–292.

Savage, M.K., Peppin, W.A. & Vetter, U.R., 1990. Shear wave anisotropy and stress direction in and near Long Valley caldera, California, 1979–1988, *J. geophys. Res.,* **95,** 11 165–11 117.

Seeber, L., Armbruster, J.G., Ozer, N., Aktar, M., Baris, S., Okaya, D., Ben-Zion, Y. & Field, E., 2000. The 1999 Earthquake Sequence along the North Anatolia Transform at the Juncture between the Two Main Ruptures, in *The 1999 İzmit and Düzce Earthquakes: preliminary results,*pp. 209–223, eds Barka *et al.* Istanbul Technical University, Istanbul.

Shih, X.R. & Meyer, R.P., 1990. Observation of shear wave splitting from nature events: South Moat of Long Valley caldera, California, June 29 to August 12, 1982, *J. geophys. Res.,* **95,** 11 179–11 196.

Silver, P.G. & Chan, W.W., 1991. Shear-wave splitting and subcontinental mantle deformation, *J. geophys. Res.,* **96,** 16 429–16 454.

Tadokoro, K. & Ando, M., 2002. Evidence for rapid fault healing derived from temporal changes in S wave splitting, *Geophys. Res. Lett.,* **29,** 6–1.

Tadokoro, K., Ando, M. & Umeda, Y., 1999. *S* wave splitting in the aftershock region of the 1995 Hyogo-ken Nanbu earthquake, *J. geophys. Res.,* **104,** 981–991.

Tadokoro, K. *et al.*, 2002. Monitoring fault healing after the 1999 Kocaeli, Turkey, earthquake, *J. Seismol.*, **6,** 411–417.

Utkucu, M., Nalbant, S.S., McCloskey, J., Steacy, S. & Alptekin, O., 2003. Slip distribution and stress changes associated with the 1999 November 12, Düzce (Turkey) earthquake (Mw = 7.1), *Geophys. J. Int.,* **153,** 229–241.

Vidale, J.E., 1986, Complex polarization analysis of particle motion, *Bull. seism. Soc. Am.*, **76,** 1393–1405.

Wessel, P. & Smith, W.H.F., 1998. New version of the Generic Mapping Tools Released, *EOS Trans. Amer. Geophys. Union*, **79,** 579.

Yilmaz, Y., Tuysuz, O., Yigitbas, E., Genc, S.C. & Sengor, A.M.C., 1997. Geology and Tectonic Evolution of the Pontides, in *Regional and Petroleum geology of the Black Sea and Surrounding Region: AAPG Memoir 68*, pp. 183–226, ed. Robinson, A.G., AAPG, Tulsa, OK, USA.

Zhang, Z. & Schwartz, S.Y., 1994. Seismic anisotropy in the shallow crust of the Loma Prieta segment of the San Andreas fault system, *J. geophys. Res.,* **99**(B5), 9651–9661.

Zinke, J. & Zoback, M.D., 2000. Structure-related and stress-induced shear-wave velocity anisotropy: observations from microearthquakes near the Calaveras Fault in central California, *Bull. seism. Soc. Am.,* **90,** 1305–1312.